

1 **Effects of fluid-rock interaction on  $^{40}\text{Ar}/^{39}\text{Ar}$**   
2 **geochronology in high-pressure rocks (Sesia-Lanzo**  
3 **Zone, Western Alps)**

4  
5  
6 **Ralf Halama<sup>1,\*</sup>, Matthias Konrad-Schmolke<sup>1</sup>, Masafumi Sudo<sup>1</sup>,**  
7 **Horst R. Marschall<sup>2</sup>, Michael Wiedenbeck<sup>3</sup>**

8  
9 <sup>1</sup> Institute of Earth and Environmental Science, University of Potsdam, Karl-Liebknecht-Str.  
10 24-25, 14476 Potsdam, Germany

11 <sup>2</sup> Woods Hole Oceanographic Institution, 266 Woods Hole Rd., Woods Hole, MA 02543,  
12 USA

13 <sup>3</sup> GFZ German Research Centre for Geosciences, Telegrafenberg, C128, 14473 Potsdam  
14

15 \* Corresponding author contact information:

16 Ralf Halama

17 University of Potsdam

18 Institute of Earth and Environmental Science

19 Karl-Liebknecht-Str. 24-25

20 14476 Potsdam

21 E-mail: [rhalama@geo.uni-potsdam.de](mailto:rhalama@geo.uni-potsdam.de)

22 Tel: +49-331-977-5783

23 Fax: +49-331-977-5700

24

25 *Accepted version, 13. October 2013*

26

## 26 **Abstract**

27

28 *In situ* UV laser spot  $^{40}\text{Ar}/^{39}\text{Ar}$  analyses of distinct phengite types in eclogite-facies  
29 rocks from the Sesia-Lanzo Zone (Western Alps, Italy) were combined with SIMS boron  
30 isotope analyses as well as boron (B) and lithium (Li) concentration data to link  
31 geochronological information with constraints on fluid-rock interaction. In weakly deformed  
32 samples, apparent  $^{40}\text{Ar}/^{39}\text{Ar}$  ages of phengite cores span a range of ~20 Ma, but inverse  
33 isochrons define two distinct main high-pressure (HP) phengite core crystallization periods of  
34 88-82 Ma and 77-74 Ma, respectively. The younger cores have on average lower B contents  
35 (~36  $\mu\text{g/g}$ ) than the older ones (~43-48  $\mu\text{g/g}$ ), suggesting that loss of B and resetting of the Ar  
36 isotopic system were related. Phengite cores have variable  $\delta^{11}\text{B}$  values (-18 to -10 ‰),  
37 indicating the lack of km scale B homogenization during HP crystallization.

38 Overprinted phengite rims in the weakly deformed samples generally yield younger  
39 apparent  $^{40}\text{Ar}/^{39}\text{Ar}$  ages than the respective cores. They also show variable effects of  
40 heterogeneous excess  $^{40}\text{Ar}$  incorporation and Ar loss. One acceptable inverse isochron age of  
41  $77.1 \pm 1.1$  Ma for rims surrounding older cores ( $82.6 \pm 0.6$  Ma) overlaps with the second  
42 period of core crystallization. Compared to the phengite cores, all rims have lower B and Li  
43 abundances but similar  $\delta^{11}\text{B}$  values (-15 to -9 ‰), reflecting internal redistribution of B and  
44 Li and internal fluid buffering of the B isotopic composition during rim growth. The  
45 combined observation of younger  $^{40}\text{Ar}/^{39}\text{Ar}$  ages and boron loss, yielding comparable values  
46 of both parameters only in cores and rims of different samples, is best explained by a selective  
47 metasomatic overprint. In low permeability samples, this overprint caused recrystallization of  
48 phengite rims, whereas higher permeability in other samples led to complete recrystallization  
49 of phengite grains.

50 Strongly deformed samples from a several km long, blueschist-facies shear zone  
51 contain mylonitic phengite that forms a tightly clustered group of relatively young apparent  
52  $^{40}\text{Ar}/^{39}\text{Ar}$  ages (64.7 to 68.8 Ma), yielding an inverse isochron age of  $65.0 \pm 3.0$  Ma. Almost  
53 complete B and Li removal in mylonitic phengite is due to leaching into a fluid. The B  
54 isotopic composition is significantly heavier than in phengites from the weakly deformed  
55 samples, indicating an external control by a high- $\delta^{11}\text{B}$  fluid ( $\delta^{11}\text{B} = +7 \pm 4$  ‰). We interpret  
56 this result as reflecting phengite recrystallization related to deformation and associated fluid  
57 flow in the shear zone. This event also caused partial resetting of the Ar isotope system and  
58 further B loss in more permeable rocks of the adjacent unit. We conclude that geochemical

59 evidence for pervasive or limited fluid flow is crucial for the interpretation of  $^{40}\text{Ar}/^{39}\text{Ar}$  data  
60 in partially metasomatized rocks.

61

62

63 **Keywords:**

64  $^{40}\text{Ar}/^{39}\text{Ar}$  geochronology, fluid-rock interaction, boron isotopes, Sesia-Lanzo Zone,  
65 metasomatism

66

# 1. Introduction

66  
67  
68  
69  
70  
71  
72  
73  
74  
75  
76  
77  
78  
79  
80  
81  
82  
83  
84  
85  
86  
87  
88  
89  
90  
91  
92  
93  
94  
95  
96  
97  
98  
99

$^{40}\text{Ar}/^{39}\text{Ar}$  geochronology is one of the most valuable tools for determining the timing of geologic events. For metamorphic rocks,  $^{40}\text{Ar}/^{39}\text{Ar}$  data are commonly used for unraveling metamorphic exhumation and tectonometamorphic timescales (Di Vincenzo et al., 2006; Beltrando et al., 2009; Wiederkehr et al., 2009; Willner et al., 2009; Warren et al., 2012a, b) as well as the timing of fluid-rock interaction processes (Boundy et al., 1997; Di Vincenzo and Palmeri, 2001; Baxter et al., 2002; Warren et al., 2011, 2012c). *In situ*  $^{40}\text{Ar}/^{39}\text{Ar}$  data with high spatial resolution in combination with textural and petrologic information are particularly powerful for obtaining information about P-T conditions, metasomatism and deformation in the history of a rock (Scaillet et al., 1990; Di Vincenzo et al., 2001, 2006; Putlitz et al., 2005; Warren et al., 2011; Willner et al., 2011).

Besides accumulation of radiogenic  $^{40}\text{Ar}$ , concentration and isotopic composition of Ar in minerals are modified by recrystallization and thermal diffusion. In general, recrystallization is the dominant mechanism for alteration of the Ar isotopic composition at lower temperatures, whereas diffusion becomes more important at higher temperatures. However, thermally induced Ar loss by diffusion through the crystal lattice is relatively ineffective in comparison with deformation and chemical reaction mechanisms (Hames and Cheney, 1997). Reactive chemical exchanges together with fluid-mediated element transport are, therefore, the main factors controlling the rate of Ar transport and distribution in a rock (Villa, 1998; Di Vincenzo et al., 2006). Intracrystalline Ar diffusion in metamorphic white mica is particularly inefficient at low temperatures and/or high pressures, and little diffusive Ar loss is expected during exhumation from such regions (Warren et al., 2012a). Hence,  $^{40}\text{Ar}/^{39}\text{Ar}$  ages from phengite in eclogite-facies rocks do not necessarily record temperature histories, but rather reflect variations in radiogenic  $^{40}\text{Ar}$  acquired during phengite formation and modified by deformation-enhanced recrystallization (Putlitz et al., 2005; Warren et al., 2012b).

In several high pressure (HP) and ultra-high pressure (UHP) rocks, apparent  $^{40}\text{Ar}/^{39}\text{Ar}$  ages that are higher than the expected ages by several tens of million years, but without geological meaning were attributed to the presence of excess  $^{40}\text{Ar}$  (Arnaud and Kelley, 1995; Sherlock and Arnaud, 1999; Giorgis et al., 2000; Baxter et al., 2002; Sherlock and Kelley, 2002). The presence of excess  $^{40}\text{Ar}$  and apparent older ages in HP/UHP rocks are thought to reflect a closed, fluid-poor system in which radiogenic Ar that was produced from detrital K-bearing phases is not removed (Kelley, 2002; Sherlock and Kelley, 2002). This

100 implies that open system conditions with a zero grain boundary Ar concentration (i.e. no  
101 accumulation of radiogenic Ar while the mineral can still exchange Ar with the intergranular  
102 fluid) cannot always be assumed in metamorphic systems (Baxter et al., 2002; Warren et al.,  
103 2012b, c). Extraneous Ar in (U)HP rocks may be derived from protoliths whose isotopic  
104 signature can survive (U)HP metamorphism and exhumation if the system is closed  
105 isotopically. In subduction-metamorphosed rocks, other stable and radiogenic isotopic  
106 systems, such as O, Sr and Nd, can preserve pre-subduction signatures without significant  
107 isotopic exchange during subduction and exhumation, especially under fluid-restricted  
108 conditions (Putlitz et al., 2000, 2005; Früh-Green et al., 2001; Halama et al., 2011). Thus it is  
109 clear that information about the extent of fluid-rock interaction and its effect on the isotopic  
110 composition of Ar is crucial for a correct interpretation of age constraints derived from  
111  $^{40}\text{Ar}/^{39}\text{Ar}$  data.

112 Boron (B) is a particularly useful element for detecting and quantifying the extent of  
113 fluid-rock interaction during metamorphism because B is a relatively mobile element in  
114 hydrous fluids (Brenan et al., 1998; Marschall et al., 2007) and a large isotopic fractionation  
115 of the two stable B isotopes ( $^{10}\text{B}$  and  $^{11}\text{B}$ ) between minerals and fluids has been observed at  
116 low temperatures (Wunder et al., 2005). The combined decrease in  $\delta^{11}\text{B}$  values and B  
117 concentrations in across-arc profiles of arc lavas is thought to reflect the effects of B isotope  
118 fractionation during progressive dehydration with increasing depth of the Wadati-Benioff  
119 zone: The residual rock becomes isotopically lighter due to the preference of the heavy  $^{11}\text{B}$   
120 isotope for the fluid and the slab-fluid flux toward the back arc steadily decreases (Ishikawa  
121 and Nakamura, 1994; Bebout et al., 1999; Rosner et al., 2003; Marschall et al., 2007).  
122 Secondary ion mass spectrometry (SIMS) analyses confirm that slab dehydration significantly  
123 lowers  $\delta^{11}\text{B}$  of subducted oceanic crust and sediments (Peacock and Hervig, 1999; Pabst et al.,  
124 2012), but there is a lack of systematic relationships with peak metamorphic conditions  
125 pointing to effects of metasomatic overprinting. Boron concentration zoning in  
126 metasomatically overprinted micas and amphiboles (Konrad-Schmolke et al., 2011b) and B  
127 isotopic zoning in tourmaline that retains information about the metamorphic fluid evolution  
128 through the metamorphic history (Bebout and Nakamura, 2003; Marschall et al., 2009)  
129 provide evidence for the sensitivity of the B system for fluid-rock interaction processes.

130 In this study, we investigate how deformation and associated fluid flux affect  
131 apparent  $^{40}\text{Ar}/^{39}\text{Ar}$  ages in a profile from a major intracrustal, blueschist-facies shear zone into  
132 adjacent eclogite-facies rocks. We have selected samples from the Sesia-Lanzo Zone  
133 (Western Alps, Italy) because these samples are well studied in their structural and textural

134 context and they show various stages of metasomatic overprinting in major and trace element  
135 mineral chemistry related to deformation in the shear zone (Babist et al., 2006; Konrad-  
136 Schmolke et al., 2011a, b). By combining elemental (B, Li) and isotopic ( $\delta^{11}\text{B}$ ) tracers of fluid  
137 flow with *in situ*  $^{40}\text{Ar}/^{39}\text{Ar}$  dates, we aim to understand the influence of HP metasomatic  
138 processes on  $^{40}\text{Ar}/^{39}\text{Ar}$  geochronology and to test whether deformation and fluid-rock  
139 interaction are the principal mechanisms for radiogenic  $^{40}\text{Ar}$  loss from white micas (Hames &  
140 Cheney, 1997). Moreover, a large geochronological database obtained from a plethora of  
141 methods provides a valuable framework for testing the  $^{40}\text{Ar}/^{39}\text{Ar}$  age information (e.g.,  
142 Oberhänsli et al., 1985; Inger et al., 1996; Reddy et al., 1996; Duchêne et al., 1997; Ruffet et  
143 al., 1997; Rubatto et al., 2011).

144  
145

## 146 2. Geologic Setting

147

148 The Western Alpine Sesia-Lanzo Zone (SLZ) is a section of polymetamorphic Austroalpine  
149 continental crust of the African-Adriatic plate that has reached eclogite-facies conditions  
150 during Alpine metamorphism. The following summary of its geologic history is based on the  
151 review by Beltrando et al. (2010) and references therein.

152 Since the Cretaceous, the Western Alps formed due to convergence between Europe  
153 and Adria, the latter considered as promontory of Africa or an independent micro-plate. The  
154 continental basement units of the SLZ originated from the Adriatic margin and form today the  
155 structurally uppermost part of an axial belt comprising continental units derived from Adriatic  
156 and European margins and oceanic units from the Mesozoic Piemonte-Liguria Ocean (Fig.  
157 1a). To the East, the SLZ is bounded by the Insubric Line and the Southern Alps, whereas  
158 sub-continental peridotites of the Lanzo Massif border the SLZ to the South. Continental units  
159 from the European margin and oceanic units from the Tethys Ocean, together part of the  
160 Penninic Domain, occur to the West of the SLZ. The subducted oceanic rocks were exhumed  
161 in the footwall of the SLZ during convergence prior to continent-continent collision (Babist et  
162 al., 2006).

163 The SLZ is subdivided into three distinct subunits based on lithology and  
164 metamorphic grade (Fig. 1a), although slightly different subdivisions have also been proposed  
165 (Venturini et al., 1994; Babist et al., 2006). The easternmost of the three SW-NE trending  
166 units is the Eclogitic Micaschist Complex (EMS), which is a polymetamorphic basement that  
167 includes paragneisses, minor metabasic rocks and marbles. Granitoids and minor gabbros

168 intruded this basement during Carboniferous and Permian times. The EMS reached eclogite-  
169 facies conditions of 1.5-2.0 GPa and 550-600 °C during Alpine metamorphism, but is  
170 internally only weakly deformed (Konrad-Schmolke et al., 2006). The eclogitic assemblages  
171 overprint relict Permian amphibolite-granulite assemblages in the EMS. The Gneiss Minuti  
172 (GM) comprise orthogneisses derived from Permian granitoids that intruded into Variscan  
173 basement and metamorphosed rocks from a Mesozoic sedimentary sequence, mainly meta-  
174 arkose with minor marble, calcschist and metachert. Alpine peak metamorphic conditions in  
175 the GM reached 1.0-1.5 GPa at 500-550 °C, but they have experienced a pervasive  
176 greenschist-facies metamorphic overprint. Along the contact between EMS and GM, the  
177 Seconda Zona Diorito-Kinzigitica (IIDK) crops out discontinuously (Fig. 1a). The IIDK  
178 represents pre-Alpine slice of lower crustal, amphibolite-facies micaschists with subordinate  
179 amounts of mafic granulites, amphibolites and marbles. Re-equilibration during Alpine  
180 metamorphism occurred under blueschist-facies conditions, but is restricted to the margins of  
181 the discrete slivers or to narrow shear zones.

182           One major shear zone separating the EMS from the GM is the Tallorno Shear Zone  
183 (TSZ) with a length of approximately 20 km and a width of 1-2 km (Fig. 1b; Konrad-  
184 Schmolke et al., 2011a). Deformation in the TSZ was active under blueschist-facies  
185 conditions, forming garnet-bearing plagioclase–epidote–sodic amphibole–paragonite–  
186 phengite mylonites (Babist et al., 2006). During juxtaposition of the two major lithologic  
187 units, contemporaneous subduction of oceanic crust from the Piemonte-Liguria Ocean  
188 provided supply of dehydration fluids. A strain- and recrystallization gradient in the EMS was  
189 induced by the displacements along and fluid flow within the TSZ. Samples were taken along  
190 a ~5 km long profile from the TSZ into the EMS in the Chiusella Valley, which cuts in NW-  
191 SE direction through the SLZ (Fig. 1b). Sample MK-99 was taken about 16 km to the NE of  
192 sample TSZR in the Nantay Valley, a tributary to the Lys Valley, and is projected onto the  
193 cross-section.

194

195

196

### 3. Petrography and Mineral Chemistry

197

198 The samples can be subdivided into weakly deformed, fine- to medium-grained rocks from  
199 the EMS unit (samples MK-30, MK-52, MK-55 and 3i) and fine-grained mylonites from the  
200 Tallorno Shear Zone (samples TSZR and MK-99). All samples, except sample 3i, were  
201 previously described and investigated for major and trace element abundances in the main

202 mineral phases by Konrad-Schmolke et al. (2011a, b), and the following summary is based on  
203 this work.

204 The EMS samples are moderately foliated and comprise two felsic gneisses (MK-30  
205 and MK-55), a mafic gneiss (MK-52) and a micaschist (3i). All EMS samples have a  
206 preserved HP mineral assemblage of quartz + phengite + omphacite (or pseudomorphs after  
207 omphacite) + sodic amphibole + garnet + rutile + paragonite. The felsic samples are rich in  
208 quartz and phengite. The micaschist (3i) contains large phengite flakes up to 0.5 cm in size.  
209 The mafic gneiss (MK-52) shows compositional banding and is dominated by sodic  
210 amphibole, garnet and omphacite. The foliation is parallel to the compositional banding and  
211 interpreted to be syn-kinematic with respect to the mylonitic blueschist-facies shear zone at  
212 the EMS-GM contact (Babist et al., 2006). Two stages of retrograde overprint in the stability  
213 field of sodic amphibole and a third, weakly developed greenschist-facies overprint were  
214 identified in the EMS samples. Both phengite and sodic amphibole show major element  
215 compositional differences between pristine cores and overprinted areas (Fig. 2a). Primary  
216 phengite cores have 3.3-3.5 Si per formula unit (p.f.u.) and  $X_{Mg}$  between 0.70 and 0.85 (Fig.  
217 2b). Chemical modifications occur at the grain boundaries and around inclusions and include  
218 a decrease in  $X_{Mg}$  to values around 0.6-0.7 (Fig. 2b), lower Na and Sr and higher Ba and Cl  
219 contents. Overprinting of phengite is occasionally associated with an increase in Si contents  
220 (Fig. 2c). Thermodynamic modeling (Konrad-Schmolke et al., 2011a) demonstrates that a  
221 significant amount of water (1.0-1.5 wt.%) must have been present on the retrograde path to  
222 maintain water saturation and to produce the newly formed rim compositions and retrograde  
223 mineral assemblages. The step-like compositional zoning contradicts a continuous  
224 thermodynamic equilibration during exhumation. Instead, it demonstrates the effects of  
225 discrete fluid-rock interaction stages during decompression and an associated modification of  
226 the major element chemistry of phengite and sodic amphibole (Konrad-Schmolke et al.,  
227 2011a, b). Overprinting in the weakly deformed EMS samples collected at some distance to  
228 the Tallorno Shear Zone is restricted to narrow, clearly separated zones along grain  
229 boundaries and fluid pathways. The rapid water re-saturation and the partial compositional  
230 equilibration of the mineral assemblage due to pervasive fluid influx along grain boundaries  
231 must have occurred under blueschist-facies conditions, since the observed phengite and  
232 amphibole rim compositions are calculated to be stable between 1.1 and 1.4 GPa (Fig. 2d).

233 The mylonitic samples from the Tallorno Shear Zone comprise a felsic (TSZR) and a  
234 mafic (MK-99), fine-grained schist. Major mineral phases are garnet + epidote + albite +  
235 phengite + sodic amphibole ± chlorite. Omphacite is lacking, but there are scarce relicts of



236 garnet and/or cores of sodic amphibole. Neither of the two mylonites shows petrographically  
237 or chemically distinct phengite rims, but relict flakes of pre-kinematic phengite occur in  
238 sample TSZR. A greenschist-facies overprint is evident from chlorite replacing garnet and  
239 chlorite + albite replacing sodic amphibole. The mylonitic rocks are well equilibrated under  
240 retrograde blueschist-facies conditions, and the minerals are compositionally more  
241 homogeneous than in the weakly deformed EMS unit. Phengite in the mylonites is typically  
242 fine-grained (5-200  $\mu\text{m}$ ), chemically homogenous with Si contents of 3.3 and 3.5 p.f.u. in  
243 felsic and mafic samples, respectively. The weakly zoned, mm-sized phengite clasts show  
244 decreasing trends in  $X_{\text{Mg}}$  from core (0.8) to rim (0.6). The small, mylonitic phengite has a  
245 major element composition and  $X_{\text{Mg}}$  similar to the rims of the large grains.

246 Boron (B) and lithium (Li) concentrations decrease systematically from phengite  
247 cores via rims in the weakly deformed samples towards the mylonitic phengites (Fig. 3a;  
248 Konrad-Schmolke et al., 2011b). The modifications were explained and successfully modeled  
249 by fluid infiltration. Initially, phengite (and amphibole) compositions equilibrated with the  
250 infiltrating fluid, so that the composition changed towards the observed rim values. In  
251 samples where fluid percolation continued, Li and B were depleted further until eventually,  
252 this leaching effect produced the low Li and B contents in the mylonitic samples. The amount  
253 of percolating fluid controlled the extent of Li and B depletion, and the retrograde fluid influx  
254 evidently increased from the weakly deformed EMS samples towards the highly deformed  
255 mylonites. Distinct fluid-rock ratios for crystallization of the overprinted rims ( $\sim 0.2$ ) and the  
256 mylonitic phengites ( $\sim 4$ ) can explain the distinct Li/B ratios. In summary, fluid-rock  
257 interaction with low fluid influx at blueschist-facies conditions led to partial re-hydration and  
258 re-equilibration of eclogite-facies mineral assemblages in the EMS, whereas the mylonites  
259 from the TSZ experienced high fluid influx and consequently a more pronounced re-  
260 equilibration.

261 Based on the distinct compositions that are related to variable degrees of fluid  
262 overprinting, the selected samples are ideally suited to study fluid-rock interaction using B  
263 isotopes. Moreover, the elevated Fe contents in phengite rims cause chemical contrasts that  
264 can be easily visualized using BSE images, so that areas most suitable for *in situ*  $^{40}\text{Ar}/^{39}\text{Ar}$   
265 analyses can be identified.

266

267

268

## 4. Analytical methods

269

#### 270 **4.1. Secondary ion mass spectrometry (SIMS) boron isotope measurements**

271 Boron isotope measurements were completed in Heidelberg and Potsdam, and  
272 although similar approaches were used, details of the different procedures are given separately  
273 below. Boron isotopic compositions of samples are reported using the  $\delta$ -notation ( $\delta^{11}\text{B}$  in ‰)  
274 relative to NBS-SRM 951, which has an assigned  $^{11}\text{B}/^{10}\text{B}$  value of 4.043627 (Catanzaro et al.,  
275 1970).

276

##### 277 4.1.1. Institut für Geowissenschaften, Universität Heidelberg

278 Boron isotope ratios of phengite were measured with a modified Cameca IMS 3f ion  
279 microprobe equipped with a primary beam mass filter. The primary ion beam was  $^{16}\text{O}^-$   
280 accelerated to 10 keV with a beam current of 30 nA, resulting in a beam diameter of  $\sim 40\ \mu\text{m}$   
281 and count rates of  $\sim 2 \times 10^4\ \text{s}^{-1}$  and  $\sim 5 \times 10^3\ \text{s}^{-1}$  for  $^{11}\text{B}$  and  $^{10}\text{B}$ , respectively. The energy  
282 window was set to 100 eV without offset. Mass resolution ( $M/\Delta M$ ) was  $\sim 1185$ . Each analysis  
283 spot was presputtered for 5 min before 200 cycles were measured with counting times of  
284 3.307 s on  $^{10}\text{B}$  and 1.660 s on  $^{11}\text{B}$ . The settling time between two different masses was 200  
285 ms, resulting in a total analysis time for one spot of  $\sim 25$  min. Instrumental mass fractionation  
286 was determined by using phengite sample Phe-80-3 (Klemme et al., 2011), which is  
287 chemically homogenous and has previously been analyzed by SIMS and TIMS yielding  $\delta^{11}\text{B}$   
288 values of  $-14.8 \pm 2.8\ \text{‰}$  (1s, n=10) and  $-13.50 \pm 0.35\ \text{‰}$  (1s, n=2), respectively (Pabst et al.,  
289 2012). The analytical uncertainty is typically  $\leq 2\ \text{‰}$  for the weakly deformed samples ( $\sim 20$ -60  
290  $\mu\text{g/g}$  B) and  $< 4\ \text{‰}$  for the low-B ( $< 10\ \mu\text{g/g}$  B) mylonitic samples, as based on the observed  
291 distribution of the 200 ratios obtained from a single measurement.

292

##### 293 4.1.2. GeoForschungsZentrum, Potsdam

294 Phengite and paragonite  $^{11}\text{B}/^{10}\text{B}$  ratios on Au-coated thin sections were determined  
295 by using a Cameca IMS 6f ion microprobe. Prior to each analysis, a 60 s at 25 nA presputter  
296 was applied in order to remove the gold coat and to establish equilibrium sputtering  
297 conditions. The mass spectrometer was operated at mass resolving power  $M/\Delta M \sim 1200$ ,  
298 sufficient to separate the isobaric interference of  $^{10}\text{B}^1\text{H}$  on the  $^{11}\text{B}$  mass station and the  $^9\text{Be}^1\text{H}$   
299 peak on  $^{10}\text{B}$  (Trumbull et al., 2009).  $^{11}\text{B}/^{10}\text{B}$  ratios were measured over 250 cycles and  
300 counting times per cycle on  $^{10}\text{B}$  and  $^{11}\text{B}$  were 2 and 4 s, respectively. A 12.5 keV  $^{16}\text{O}^-$  primary  
301 beam was focused to about 35  $\mu\text{m}$  diameter on the sample surface. The beam current was set  
302 to 25 nA. A 150  $\mu\text{m}$  diameter contrast aperture, a 1800  $\mu\text{m}$  field aperture (equivalent to a field  
303 of view 150  $\mu\text{m}$  in diameter) and 50 eV energy window were used without voltage offset.

304 Instrumental mass fractionation was corrected using NIST SRM 610 glass; as this is not well  
305 matched to the matrices studied in this investigation we cannot rule out the presence of some  
306 systematic offset in the data reported here (see also Rosner et al. (2008) for a discussion of  
307 matrix effects within silicate glasses). The reference material was analyzed at the start and end  
308 of each daily section and before changing of samples. The analytical uncertainty is  $\leq 2\%$  (1s)  
309 for samples with moderate B contents and  $<6\%$  for mylonitic samples with very low B  
310 contents ( $< 5 \mu\text{g/g B}$ ), as based on the 250 cycles of data which were collected.

311

312

#### 313 **4.2. *In situ* $^{40}\text{Ar}/^{39}\text{Ar}$ analyses**

314  $^{40}\text{Ar}/^{39}\text{Ar}$  dating was carried out at the Institute of Earth and Environmental Science,  
315 Universität Potsdam, after neutron activation of polished thick sections (1 cm diameter and  
316 less than 1 mm thickness) at the Geesthacht Neutron Facility (GeNF) of the GKSS research  
317 center in Geesthacht, Germany. Details about sample preparation, neutron activation and Ar  
318 isotopic analyses are given in Wiederkehr et al. (2009) and Wilke et al. (2010) and are  
319 summarized here. Back-scattered electron images of the sections were obtained to select the  
320 most suitable phengite core and rim locations for the *in situ* Ar isotopic analyses. Samples  
321 were wrapped in aluminium foil and placed in capsules made of 99.999% Al. The capsules  
322 were shielded with 0.5 mm thick Cd foil and irradiated with fast neutrons at a flux rate of  $1 \times$   
323  $10^{12} \text{ n cm}^{-2} \text{ s}^{-1}$  for 97 h. Together with the samples, Fish Canyon Tuff (FCT) sanidine, FC3  
324 sanidine, was irradiated to monitor neutron flux and its spatial variation and to derive J  
325 values. The FC3 sanidine was prepared by the Geological Survey of Japan (GSJ) and the age  
326 of 27.5 Ma was determined by K-Ar dating of FC3 biotite at GSJ (Uto et al., 1997; Ishizuka,  
327 1998). This age of 27.5 Ma is consistent with the age obtained by the USGS (Lanphere and  
328 Baadsgaard, 2001) and both laboratories determined the ages by first principles calibration  
329 (Lanphere and Dalrymple, 2000). The true age of the FCT sanidine is in dispute, and  
330 alternative ages of 27.93 Ma (Channell et al., 2010), 28.02 Ma (Renne et al. 1998), 28.201 Ma  
331 (Kuiper et al., 2008) and 28.305 Ma (Renne et al., 2010) were also reported. Although higher  
332 values are apparently more compatible with U-Pb ages, the age used here is based on the  
333 value determined by first principles calibrations, which have been independently verified by  
334 different laboratories in Japan and the US (Lanphere and Dalrymple, 2000; Lanphere, 2004).  
335 Moreover,  $\text{K}_2\text{SO}_4$  and  $\text{CaF}_2$  crystals were irradiated for the correction of Ar isotope  
336 interferences produced by reactions of the neutron flux with K or Ca in the samples. SORI93  
337 biotite ( $92.6 \pm 0.6 \text{ Ma}$ ; Sudo et al., 1998) and HD-B1 biotite ( $24.2 \pm 0.3 \text{ Ma}$ , Hess and Lippolt,

338 1994;  $24.18 \pm 0.09$  Ma, Schwarz and Trieloff, 2007) were irradiated and analyzed to check  
339 accuracy and precision of the age determinations.

340 The Ar isotopic analytical system consists of a New Wave Gantry Dual Wave laser ablation  
341 system, an ultrahigh-vacuum purification line, and a Micromass 5400 noble gas mass  
342 spectrometer (Wiederkehr et al., 2009; Willner et al., 2011). The laser with a frequency-  
343 quadrupled wavelength of 266 nm was operated with a beam size of 50-80  $\mu\text{m}$ , a repetition  
344 rate of 10 Hz and a continuous duration of ablation for 2 min to extract gas from the samples.  
345 For the weakly deformed EMS samples, this spot size was sufficiently small to analyze single  
346 spots or lines in a certain domain (core or rim) of the phengite crystals. Only in the  
347 mylonitized samples, where the phengite grain size is smaller, line analyses include domains  
348 with several phengite crystals and some matrix material. The extracted gas is purified in the  
349 ultra-high vacuum line via SAES getter pumps and a cold trap for 10 min. Two Zr-Al SAES  
350 getters are used for the purification of sample gas at 400  $^{\circ}\text{C}$  and room temperature,  
351 respectively. The cold trap is kept at  $-90^{\circ}\text{C}$  through ethanol cooled by an electric immersion  
352 cooler equipped with a stainless steel cooling finger. The high sensitivity, low background  
353 sector-type mass spectrometer used for Ar isotopic analysis is equipped with an electron  
354 multiplier pulse counting system for analyzing small amounts of Ar. Blanks were run at the  
355 start of each session and after every three unknowns. The raw data were corrected for  
356 procedural blank contributions, mass discrimination by analysis of atmospheric Ar, and decay  
357 of radiogenic  $^{37}\text{Ar}$  and  $^{39}\text{Ar}$  isotopes produced by irradiation. For blank correction, averages  
358 of the blanks measured before and after the unknowns were used. Beam intensities during  
359 blank measurements typically were  $4.3\text{-}6.5 \times 10^{-5}$  V for  $^{40}\text{Ar}$ ,  $4.3\text{-}7.5 \times 10^{-8}$  V for  $^{39}\text{Ar}$ ,  $6.6 \times$   
360  $10^{-8} - 1.8 \times 10^{-7}$  V for  $^{38}\text{Ar}$ ,  $3.2\text{-}5.7 \times 10^{-7}$  V for  $^{37}\text{Ar}$  and  $4.6\text{-}6.5 \times 10^{-7}$  V for  $^{36}\text{Ar}$ . Beam  
361 intensity ratios of unknowns to blanks were 5-20 for  $^{40}\text{Ar}$ , 380-1130 for  $^{39}\text{Ar}$ , 1.7-5.0 for  $^{38}\text{Ar}$ ,  
362  $< 0.3$  for  $^{37}\text{Ar}$  and 0.1-1.5 for  $^{36}\text{Ar}$ . For atmospheric and mass discrimination corrections,  
363 295.5 and 0.1869 were used as atmospheric  $^{40}\text{Ar}/^{36}\text{Ar}$  and  $^{38}\text{Ar}/^{36}\text{Ar}$  ratios, respectively (Nier  
364 et al. 1950). Using a more recently determined alternative atmospheric ratio of 298.56 for  
365  $^{40}\text{Ar}/^{36}\text{Ar}$  (Lee et al., 2006) would have only minuscule effects on the calculated  $^{40}\text{Ar}/^{39}\text{Ar}$   
366 dates. Interference corrections of  $^{36}\text{Ar}$  produced from  $^{40}\text{Ca}$ ,  $^{39}\text{Ar}$  produced from  $^{42}\text{Ca}$ , and  $^{40}\text{Ar}$   
367 produced from  $^{40}\text{K}$  were also applied. Calculation of ages and errors was performed following  
368 Uto et al. (1997) using the total  $^{40}\text{K}$  decay constant of  $5.543 \times 10^{-10} \text{ a}^{-1}$  as well as decay  
369 constants of  $1.978 \times 10^{-2} \text{ d}^{-1}$  for  $^{37}\text{Ar}$  and  $2.58 \times 10^{-3} \text{ a}^{-1}$  for  $^{39}\text{Ar}$ . Due to the Cd shielding (0.5  
370 mm Cd) employed, the sample is shielded from thermal neutrons during irradiation. Hence,  
371 the levels of  $^{38}\text{Ar}_{\text{Cl}}$ , produced via thermal neutron activation of  $^{37}\text{Cl}$ , are very low (see

372 McDougall and Harrison (1999) for discussion) and  $^{38}\text{Ar}_{\text{Cl}}/^{39}\text{Ar}_{\text{K}}$  ratios could not be used to  
373 trace Cl-rich components. All Ar isotope data are given in the Electronic Annex.

374

375

376

## 5. Results

377

### 5.1. Boron isotopes

379 Boron isotopic compositions of phengite (Table 1) were analyzed in locations that  
380 had been selected based on the BSE images in order to distinguish between cores and rims in  
381 the partially overprinted EMS samples. Overall,  $\delta^{11}\text{B}$  values range from -20 to +6 ‰, and  
382 there is a significant difference between the weakly deformed samples with exclusively  
383 negative  $\delta^{11}\text{B}$  (-20 to -6 ‰) and the mylonitic shear zone samples that have a broader range of  
384 typically heavier and partly positive  $\delta^{11}\text{B}$  values (-11 to +6 ‰).

385 The two felsic gneisses (samples MK-30 and MK-55) have overlapping  $\delta^{11}\text{B}$  in  
386 phengite cores and overprinted rims (Table 1; Fig. 3). However, the overall  $\delta^{11}\text{B}$  values vary  
387 between the two samples: Phengite in gneiss MK-55 ( $\delta^{11}\text{B}_{\text{cores}} = -10.0 \pm 0.9$  ‰ [n=3];  $\delta^{11}\text{B}_{\text{rims}}$   
388  $= -9.5 \pm 1.2$  ‰ [n=3]) is isotopically heavier compared to phengite in gneiss MK-30 ( $\delta^{11}\text{B}_{\text{cores}}$   
389  $= -14.6 \pm 0.8$  ‰ [n=6];  $\delta^{11}\text{B}_{\text{rims}} = -13.4 \pm 1.3$  ‰ [n=7]). The micaschist (sample 3i) has  $\delta^{11}\text{B}$   
390 values similar to sample MK-30 with  $\delta^{11}\text{B}_{\text{cores}} = -14.3 \pm 2.2$  ‰ [n=6] and  $\delta^{11}\text{B}_{\text{rims}} = -15.3 \pm 2.5$   
391 [n=7]. In contrast, the weakly deformed metabasite (sample MK-52) has isotopically lighter  
392 phengite cores ( $\delta^{11}\text{B}_{\text{cores}} = -17.6 \pm 3.4$  ‰ [n=7]) than rims  $\delta^{11}\text{B}_{\text{rims}} = -11.3 \pm 5.7$  ‰ [n=6]),  
393 although there is some overlap as well. There is no systematic trend in the three samples  
394 relative to the distance to the shear zone. In the mafic mylonite (sample MK-99),  $\delta^{11}\text{B}$  ranges  
395 from -7 to +4 ‰ (average  $\delta^{11}\text{B} = -1.2 \pm 3.2$  ‰ [n=12]). Phengite from the felsic mylonite  
396 (sample TSZR) is isotopically most heterogeneous and shows a spread from -11 to +6 ‰  
397 (average  $\delta^{11}\text{B} = -2.3 \pm 5.3$  ‰ [n=9]). The highly negative  $\delta^{11}\text{B}$  values down to -20.4 ‰  
398 observed in the EMS samples are remarkable, as they are significantly below the typical  
399 crustal range ( $-10 \pm 3$  ‰; Marschall and Jiang, 2011) and >80% of all metamorphic minerals  
400 measured in other SIMS studies fall into the range -10 to -2 ‰ (Peacock and Hervig, 1999;  
401 Pabst et al., 2012).

402

403

### 5.2. Apparent $^{40}\text{Ar}/^{39}\text{Ar}$ ages

404

405 The apparent  $^{40}\text{Ar}/^{39}\text{Ar}$  ages vary widely and range overall from 57 Ma to 133 Ma  
406 with significant variation both within individual samples and among the specific phengite  
407 types (cores, rims and mylonitic phengite) (Electronic Annex). Note that there will be a  
408 systematic shift towards older ages by 1.5-3% if one of the alternative values for the age of  
409 the FCT sanidine standard is used. For the weakly deformed EMS samples, apparent  
410  $^{40}\text{Ar}/^{39}\text{Ar}$  ages of phengite cores cluster in the range 90–70 Ma (Fig. 4). Although there is  
411 overlap between core and rim ages, the latter tend to lower values. The most distinct  
412 separation of core and rim ages occurs in the micaschist (sample 3i) at ~70 Ma (Fig. 4). Relict  
413 cores exhibit a spread of 12 Ma from 82 to 70 Ma with an average of ~75 Ma, whereas  
414 overprinted rims yield apparent  $^{40}\text{Ar}/^{39}\text{Ar}$  ages from 57 to 69 Ma, averaging ~62 Ma (Table  
415 2). In the other EMS samples, the apparent  $^{40}\text{Ar}/^{39}\text{Ar}$  ages of phengite cores and rims,  
416 respectively, are 92–69 Ma and 88–64 Ma for felsic gneiss MK-30, 88–77 and 86–72 Ma for  
417 felsic gneiss MK-55, and 88–82 and 83–79 Ma for mafic gneiss MK-52. In both felsic  
418 gneisses, the bulk of the phengite core data falls above ~76 Ma and the respective averages  
419 are 84–81 Ma (Table 2), whereas the majority of the overprinted rims ranges in age from 70  
420 to 80 Ma (Fig. 4). The two samples from the TSZ show a larger scatter of apparent  $^{40}\text{Ar}/^{39}\text{Ar}$   
421 ages than the EMS samples (Fig. 5). In the mafic mylonite (sample MK-99), the ages cluster  
422 from 90-82 Ma, as ages <80 Ma are completely lacking and three values of ~93 Ma, ~100 Ma  
423 and ~111 Ma appear as outliers. The felsic mylonite (sample TSZR) exhibits a tightly  
424 clustered group of five apparent  $^{40}\text{Ar}/^{39}\text{Ar}$  ages in the range 68.6–64.7 Ma for mylonitic  
425 phengite. The remaining analyses, predominantly obtained in large phengite flakes, yield  
426 values from 133 to 79 Ma, the widest range observed in any of the samples.

427

428

### 429 **5.3. Inverse isochrons**

430 Inverse isochron ( $^{36}\text{Ar}/^{40}\text{Ar}$  vs.  $^{39}\text{Ar}/^{40}\text{Ar}$ ) diagrams were used in conjunction with  
431 frequency distribution plots to evaluate the age significance of the  $^{40}\text{Ar}/^{39}\text{Ar}$  data (Table 2,  
432 Figs. 4, 5). Inverse isochrons were calculated separately for distinct phengite regions (cores,  
433 rims and mylonitic phengite) that potentially reflect distinct ages. In two cases, obvious  
434 outliers were a priori excluded (suspiciously young and old dates of ~69 Ma for MK-55-2  
435 cores and ~111 Ma for MK-99-f, respectively). In addition to the MSWD value, we use the  $\chi^2$   
436 test and determined the probability of occurrence (p) as statistical tools for evaluating the  
437 reliability of the inverse isochron age information (Table 2; see Baksi (1999, 2006) for  
438 details). If  $p < 0.05$ , excess scatter of data points relative to the expected scatter is

439 demonstrated. If  $p > 0.05$ , the probability that the deviation from the expected result is due to  
440 chance only is 5% or more, which is generally considered as acceptable (Baksi, 2006).

441 For phengite cores in the weakly deformed EMS samples, there is a clear distinction  
442 in inverse isochron ages between the felsic gneisses (samples MK-30 and MK-55) and the  
443 micaschist (sample 3i). The gneisses yield inverse isochron ages of  $82.6 \pm 0.6$ ,  $83.6 \pm 0.7$ ,  $84.8$   
444  $\pm 0.7$  and  $85.0 \pm 3.3$  Ma. All of the corresponding initial  $^{40}\text{Ar}/^{36}\text{Ar}$  ratios are typically within  
445 10% uncertainty of the atmospheric value (295.5) and/or overlap this value within error.  
446 MSWD values are moderate to high (1.9–4.7), but three of the four inverse isochrons yield  $p$   
447 values  $< 0.02$ . The inverse isochron ages show good agreement with average and weighted  
448 averages of single spot ages (Table 2). The small number of data points for the mafic gneiss  
449 (MK-52) renders the calculation of a reasonable inverse isochron impossible, but averages of  
450 single spots are similar to those determined from the two felsic gneisses. In contrast, the  
451 micaschist yields significantly younger inverse isochron ages of  $75.8 \pm 0.9$ ,  $75.3 \pm 0.7$  and  $74.6$   
452  $\pm 0.7$  Ma. Two of those inverse isochrons result in relatively low MSWD values (1.6 and 1.8)  
453 associated with high  $p$  values ( $> 0.09$ ).

454 Inverse isochron ages derived for phengite rims of EMS samples are highly variable.  
455 Several very young ages, ( $52.4 \pm 4.6$  Ma,  $57.3 \pm 1.1$  Ma,  $60.2 \pm 1.4$  Ma), more than 20 Ma  
456 younger than ages calculated for the cores, are linked to initial  $^{40}\text{Ar}/^{36}\text{Ar}$  ratios that are much  
457 higher ( $> 440$ ) than the atmospheric ratio (295.5). In contrast, one relatively old inverse  
458 isochron age ( $88.7 \pm 1.1$  Ma) results in a much lower initial  $^{40}\text{Ar}/^{36}\text{Ar}$  ratio (207). Other  
459 inverse isochrons yield near-atmospheric initial  $^{40}\text{Ar}/^{36}\text{Ar}$  ratios, and the corresponding ages  
460 ( $80.2 \pm 2.2$  Ma,  $77.1 \pm 1.1$  Ma,  $72.8 \pm 3.5$  Ma) are slightly younger than the phengite core ages  
461 of the felsic gneisses but partly overlap with the core ages from the micaschist. The two  
462 phengite rim inverse isochrons, which yield ages that are similar to those from micaschist  
463 phengite cores, have fairly low MSWD (2.2 and 1.3) and high  $p$  values (0.11 and 0.25). Both  
464 of these were calculated for the felsic gneiss MK-55, which therefore has an average age  
465 difference between cores and rims of about 8 Ma.

466 No consistent age information is obtained for two discs of the mafic mylonite (sample  
467 MK-99). Inverse isochron ages are quite distinct ( $81.6 \pm 1.4$  and  $62.3 \pm 2.6$  Ma), but both have  
468 initial  $^{40}\text{Ar}/^{36}\text{Ar}$  ratios (417 and 954) well above the atmospheric value. Calculations result in  
469 moderately high MSWD ( $\geq 2.6$ ) and rather low  $p$  values ( $\leq 0.01$ ). In contrast, the tightly  
470 clustered group of apparent  $^{40}\text{Ar}/^{39}\text{Ar}$  ages around 69–64 Ma from the felsic mylonite (sample  
471 TSZR) yields a well-defined inverse isochron age of  $65.0 \pm 3.0$  Ma with a  $(^{40}\text{Ar}/^{36}\text{Ar})_i$  ratio of  
472  $306 \pm 19$ , overlapping the atmospheric ratio (Fig. 5). The statistical parameters, MSWD = 1.0

473 and  $p = 0.392$ , point to a highly reliable age information. The six older dates from the felsic  
474 mylonite with a large scatter in apparent  $^{40}\text{Ar}/^{39}\text{Ar}$  ages yield no statistically acceptable  
475 inverse isochron age.

476

477

478

## 6. Discussion

479

### 6.1. Significance of the $^{40}\text{Ar}/^{39}\text{Ar}$ ages

480

481  
482 *In situ* laser spot analyses provide total gas ages for the individual spots, unlike step-  
483 heating analyses, where heterogeneities in the Ar isotopic composition may be identified by  
484 the release of different Ar components at different temperatures. Therefore, we constructed  
485 inverse isochron diagrams from spot analyses that are considered to represent identical ages in  
486 order to identify excess  $^{40}\text{Ar}$  and potential effects of Ar loss. In inverse isochron diagrams,  
487 trapping of an excess  $^{40}\text{Ar}$  component with a  $^{36}\text{Ar}/^{40}\text{Ar}$  ratio lower than the atmospheric ratio  
488 (0.003384) causes displacement of data points to lower  $^{36}\text{Ar}/^{40}\text{Ar}$  ratios (Kuiper, 2002). Since  
489 incorporation of excess  $^{40}\text{Ar}$  is commonly heterogeneous (Sherlock and Kelley, 2002; Warren  
490 et al., 2011), scattering of data points is likely to occur, preventing the calculation of a precise  
491 inverse isochron. Argon loss, on the other hand, causes data points to move towards higher  
492  $^{39}\text{Ar}/^{40}\text{Ar}$  values because  $^{39}\text{Ar}$ , which is produced in the nuclear reactor from  $^{39}\text{K}$ , is not  
493 affected by Ar loss from the mineral (Kuiper, 2002). Hence, Ar loss will lead to younger  
494 apparent ages. If the Ar loss is complete, the timing of this event or the end of the Ar loss  
495 episode can be determined. However, if the Ar loss is incomplete, the inverse isochron age is  
496 geologically meaningless and will yield values between the initial age and the age when the  
497 Ar loss stopped (Kuiper, 2002).

498  $^{40}\text{Ar}/^{39}\text{Ar}$  ages in metamorphic rocks have traditionally been interpreted as cooling ages  
499 below the Ar closure temperature. However, a single closure temperature is unlikely to be  
500 applicable to metamorphism during rapid orogenic cycles (Warren et al., 2012a), which have  
501 presumably occurred in the SLZ (Rubatto et al., 2011). It is now established that  
502 recrystallization is the main Ar transfer mechanism within and between minerals in a  
503 metamorphic rock, and thermal diffusion is less important than fluid flow and deformation for  
504 isotope transport (Villa, 1998). Argon thermal diffusion in white mica is particularly  
505 inefficient in low- $T$  and/or high- $P$  regions, where Ar will be largely retained and little Ar is  
506 lost by thermal diffusion alone during exhumation (Warren et al., 2012a). Hence,  $^{40}\text{Ar}/^{39}\text{Ar}$



507 ages from phengite in eclogite-facies rocks record crystallization and may even preserve  
508 discrete P-T stages and a record of the deformation history (Di Vincenzo et al., 2001; Putlitz  
509 et al., 2005; Warren et al., 2012b), but only where a zero-concentration of Ar can be  
510 demonstrated and excess  $^{40}\text{Ar}$  is a negligible factor (Di Vincenzo et al., 2006; Warren et al.,  
511 2012a).

512 For the investigated samples from the SLZ, the presence of a fluid phase is  
513 prerequisite for sufficiently fast element transport that is necessary to cause the observed  
514 steep compositional gradients in phengite and amphibole and thermally induced volume  
515 diffusion as the main mechanism for the overprint can be excluded (Konrad-Schmolke et al.,  
516 2011a). Additional evidence for fluid-triggered compositional modifications comes from the  
517 observation that chemical re-equilibration in the EMS samples is restricted to fluid pathways,  
518 such as grain boundaries and brittle fractures.

519

520

#### 521 6.1.1. Phengite cores in weakly deformed EMS samples

522 For all phengite cores, several data points show deviations from the best-fit inverse  
523 isochron. This scatter may be due to (i) mixing of Ar from relict and overprinted areas during  
524 analysis, (ii) excess  $^{40}\text{Ar}$  incorporation, (iii) Ar loss, and (iv) different crystallization ages due  
525 to prolonged crystallization. Mixing of different crystal areas was avoided by conducting line  
526 analyses with total ablation depths  $\leq 20\ \mu\text{m}$ , which allowed for good spatial control on the  
527 sample surface and circumvented drilling through the desired region concerning depth. Initial  
528  $^{40}\text{Ar}/^{36}\text{Ar}$  ratios of the inverse isochrons are similar to the atmospheric ratio (Fig. 4, Table 2)  
529 so that there is no indication of a trapped excess  $^{40}\text{Ar}$  component. There are also no systematic  
530 changes in apparent ages as a function of distance from the shear zone. Fossilized radiogenic  
531 Ar waves can occur on both regional and local scale related to different geological structures  
532 (Hyodo and York, 1993; Smith et al. 1994), but the similarity of apparent phengite core ages  
533 in three samples at variable distances from the shear zones argues against the presence of such  
534 a phenomenon, and the non-systematic age variation in relation to the distance from the shear  
535 zone is more likely related to fluid-mediated Ar diffusion properties of the rock (Baxter et al.,  
536 2002). Argon loss is a possible explanation for a few data points that plot to the right of the  
537 inverse isochron and yield relatively young apparent  $^{40}\text{Ar}/^{39}\text{Ar}$  ages, but it is an unlikely  
538 explanation considering the predominantly smooth age distribution displayed by the data.  
539 Hence, we concluded that the deviation from the inverse isochron and the spread of apparent  
540  $^{40}\text{Ar}/^{39}\text{Ar}$  ages was caused by an extended period of crystallization that lasted for several

541 million years. Continuous recrystallization and/or resetting has also been advocated to explain  
542 a large variability in white mica  $^{40}\text{Ar}/^{39}\text{Ar}$  ages ( $\sim 14$  Ma) from metamorphic rocks of the  
543 Attic-Cycladic belt (Bröcker et al., 2013), and similarly large spreads in ages, from a few Ma  
544 to  $\geq 20$  Ma, were reported from different parts of the Sanbagawa HP belt in Japan (Itaya et al.,  
545 2011). Based on the inverse isochron ages of the felsic gneisses, the minimal time span for the  
546 HP crystallization episode of the phengite cores in the EMS unit is from 88 to 82 Ma. The  
547 frequency distribution plot shows that apparent  $^{40}\text{Ar}/^{39}\text{Ar}$  phengite core ages in the micaschist  
548 are distinctly younger. Although individual phengite core analyses of the gneisses and the  
549 micaschist overlap in age, the inverse isochrons of the micaschist confirm a distinctly younger  
550 period of (re)crystallization, lasting from  $\sim 77$  to  $\sim 74$  Ma.

551 Overlap of phengite  $^{40}\text{Ar}/^{39}\text{Ar}$  ages with U-Pb and Lu-Hf geochronological data is often  
552 taken as evidence that  $^{40}\text{Ar}/^{39}\text{Ar}$  ages record specific crystallization events and not cooling  
553 (Putlitz et al., 2005; Warren et al., 2012b). In the Sesia-Lanzo Zone and in particular for the  
554 EMS unit, a large number of Rb-Sr,  $^{40}\text{Ar}/^{39}\text{Ar}$  and U/Th-Pb and Lu-Hf geochronological data  
555 have been obtained (Fig. 6; Inger et al., 1996; Reddy et al., 1996; Duchêne et al., 1997; Ruffet  
556 et al., 1995; 1997; Rubatto et al., 1999; 2011). The  $^{40}\text{Ar}/^{39}\text{Ar}$  phengite core ages from the  
557 gneisses in the EMS are older than an U-Pb zircon age of  $78.5 \pm 0.9$  Ma that was interpreted to  
558 reflect the timing of HP metamorphism. They are also slightly older than the bulk of  
559 previously obtained laser spot  $^{40}\text{Ar}/^{39}\text{Ar}$  ages (68–77 Ma),  $^{40}\text{Ar}/^{39}\text{Ar}$  plateau ages (66–77 Ma)  
560 and total  $^{40}\text{Ar}/^{39}\text{Ar}$  ages (65–79 Ma) (Ruffet et al., 1995; 1997; Inger et al., 1996). Beltrando et  
561 al. (2010) critically remark that published EMS  $^{40}\text{Ar}/^{39}\text{Ar}$  ages older than 70 Ma are often  
562 considered as ‘anomalous’ and discarded as being related to excess  $^{40}\text{Ar}$ , even when no  
563 assessment of the presence of such a component was performed. The inverse isochron ages in  
564 combination with the near-atmospheric  $^{40}\text{Ar}/^{36}\text{Ar}$  ratios obtained from the inverse isochrons in  
565 this study indicates that these ages have geologic relevance. Moreover, overlap of the  
566  $^{40}\text{Ar}/^{39}\text{Ar}$  phengite core ages with an Rb-Sr isochron age of  $85 \pm 1$  Ma (Oberhänsli et al.,  
567 1985) and with U/Th-Pb allanite ages of  $\sim 85 \pm 2$  Ma (Regis et al., in press) demonstrate that  
568 there was an episode of HP crystallization during that time. Phengite crystallization from 88–  
569 82 Ma is also consistent with  $^{40}\text{Ar}/^{39}\text{Ar}$  ages of 92–82 Ma in detrital phengites from Tertiary  
570 sediments in the Piemonte Basin (Carrapa and Wijbrans, 2003).

571 The younger age of 77–74 Ma obtained from phengite cores of the micaschist point  
572 to full recrystallization several million years after the HP crystallization episode. This age is  
573 compatible with U-Pb zircon and U/Th-Pb allanite ages of  $78.5 \pm 0.9$ ,  $76.8 \pm 0.9$  and  $75.6 \pm 0.8$   
574 Ma from EMS rocks (Rubatto et al., 2011) and a U-Pb zircon age of  $76 \pm 1$  Ma from a

575 metamorphic vein within the EMS (Rubatto et al., 1999). Similar  $^{40}\text{Ar}/^{39}\text{Ar}$  plateau ages were  
576 also obtained both in the EMS ( $73.6 \pm 0.3$  to  $76.9 \pm 0.6$  Ma; Ruffet et al., 1995) and in the  
577 Pillonet Klippe ( $73.8 \pm 0.7$  to  $75.6 \pm 0.7$  Ma; Cortiana et al., 1998), which structurally belongs  
578 to the SLZ. The location of the micaschist in the middle of our structural profile is  
579 incompatible with a P-T path that is significantly different to the other samples investigated.  
580 Instead, it suggests complete resetting of the Ar isotope system in the micaschist during fluid  
581 flow at HP conditions. The gneisses were less affected, most likely because the micaschist  
582 had a higher permeability that facilitated fluid flux. This scenario agrees well with the  
583 occurrence of a vein reported in Rubatto et al. (1998), in which zircon crystallized in  
584 equilibrium with a metamorphic fluid at the same time.

585

586

#### 587 6.1.2. Overprinted phengite rims in weakly deformed EMS samples

588 It is evident from petrographic observations that the overprinted rims must have  
589 formed after phengite core crystallization, but inverse isochrons of the rims yield very  
590 inconsistent results (Fig. 4; Table 2). Some show relatively young inverse isochron ages (<60  
591 Ma) coupled to  $(^{40}\text{Ar}/^{36}\text{Ar})_i$  values that are much higher than the atmospheric ratio (e.g. MK-  
592 30-1 and 3i-Ar6); others show ages that are higher than the respective core ages and have low  
593  $(^{40}\text{Ar}/^{36}\text{Ar})_i$  values (e.g. MK-52-1). These features combined can best be explained by a  
594 combination of heterogeneous excess  $^{40}\text{Ar}$  incorporation and Ar loss that prevented the  
595 extraction of reliable age information. The incorporation of excess  $^{40}\text{Ar}$  is common in rocks  
596 with low permeability (Warren et al., 2012) and Ar depletion during low- $T$  deformation is  
597 also a common phenomenon (Itaya et al., 2011). However, several inverse isochrons (e.g.  
598 MK-55-1, MK-55-2) provide statistically reliable ( $p > 0.1$ ) ages of  $\sim 77$ – $73$  Ma with initial  
599  $^{40}\text{Ar}/^{36}\text{Ar}$  ratios close to the atmospheric ratio. This age is consistent with the metamorphic  
600 evolution of the rocks and interpreted to reflect a distinct episode of crystallization. It most  
601 likely represents a first phase of metamorphic overprint, which has been identified in EMS  
602 samples based on compositional modifications in omphacite, sodic amphibole and phengite  
603 (Konrad-Schmolke et al., 2011a).

604 Overprinted phengite rim ages of  $77$ – $73$  Ma are similar to phengite core ages from  
605 the micaschist, supporting the view that complete resetting of the Ar isotope system in the  
606 micaschist was contemporaneous with a partial overprint in the less permeable gneisses.  
607 Crystallization ages of  $75.6 \pm 0.8$  Ma for allanite cores,  $76.8 \pm 0.9$  Ma for metamorphic zircon  
608 rims (Rubatto et al., 2011) and  $76 \pm 1$  Ma for vein zircon (Rubatto et al., 1999) support the

609 interpretation of a distinct crystallization period during early exhumation of the EMS unit, as  
610 discussed in the preceding section. This first overprinting and recrystallization event must  
611 have occurred after HP crystallization at 88–82 Ma, but still at blueschist-facies conditions.  
612 The geochemical evidence for fluid-induced recrystallization of overprinted domains of the  
613 phengite grains is in excellent agreement with resetting of zircon ages and ensuing expulsion  
614 of radiogenic Pb due to fluid circulation (Gebauer and Grünenfelder, 1976). There is also  
615 evidence for later metasomatic fluid flow, presumably from the shear zone into the EMS  
616 country rocks. Phengite rims in the micaschist were affected by Ar loss, resulting in apparent  
617  $^{40}\text{Ar}/^{39}\text{Ar}$  ages <70 Ma down to ~57 Ma, and there is one apparent  $^{40}\text{Ar}/^{39}\text{Ar}$  rim age of  $64 \pm 8$   
618 Ma in a felsic gneiss (Electronic Annex). Later recrystallization and element redistribution is  
619 also indicated by the  $63.6 \pm 0.8$  Ma Rb-Sr isochron age derived from coexisting albite and  
620 phengite in the mafic gneiss (Babist et al., 2006), which indicates that a second metasomatic  
621 overprint has affected the weakly deformed EMS samples. Yet, this event was not strong  
622 enough to reset the Ar isotope system. The non-pervasive nature of the metasomatic  
623 alterations demonstrates that fluid flow and deformation were focused into the shear zone.  
624 Consequently, this second event significantly affected the relatively permeable rocks, such as  
625 the micaschist, whereas traces of this event are only sporadic in the gneisses.

626

627

### 628 6.1.3. Mylonitic phengite in samples from the Tallorno Shear Zone

629 Five analyses from the felsic mylonite (sample TSZR) with relatively young and tightly  
630 clustered apparent ages (64.7–68.8 Ma) form a well-defined inverse isochrons without any  
631 indication of excess  $^{40}\text{Ar}$  that yields a statistically reliable  $^{40}\text{Ar}/^{39}\text{Ar}$  age of  $65.0 \pm 3.0$  Ma (Fig.  
632 5). These mylonitic phengites date recrystallization and fluid flow in the shear zone,  
633 representing a second phase of blueschist-facies overprint reflected in replacement of  
634 omphacite by blueschist-facies minerals (Konrad-Schmolke et al., 2011a). This age overlaps  
635 with U-Pb zircon ages from eclogitic micaschists ( $65 \pm 3$  Ma and  $66 \pm 1$  Ma) and with a U-Pb  
636 zircon metamorphic rim age from an eclogite ( $65 \pm 5$  Ma) in the EMS unit (Inger et al., 1996;  
637 Rubatto et al., 1999). A  $^{40}\text{Ar}/^{39}\text{Ar}$  phengite plateau age of  $65.9 \pm 0.4$  Ma and concordant Rb-Sr  
638 phengite – whole rock isochron ages ( $64.2 \pm 2.5$  Ma) were also interpreted as crystallization  
639 ages (Ruffet et al., 1997). They are also similar to the Rb-Sr isochron age of  $63.6 \pm 0.8$  Ma  
640 (Babist et al., 2006) and to several K-Ar ages between  $61 \pm 4$  and  $63 \pm 3$  Ma (Oberhänsli et al.,  
641 1985). The consistency of age data obtained by different methods provides strong evidence  
642 for a discrete event in the history of the SLZ causing crystallization of mylonitic phengite,

643 zircon rims and albite (Fig. 6). Partial recrystallization occurred under blueschist-facies  
644 conditions and is related to deformation and shearing in the TSZ. These findings are in line  
645 with the significant influence of deformation on Ar diffusion by creating a network of fast  
646 diffusion pathways and causing a decrease in the effective length scale of Ar diffusion  
647 (Kramar et al., 2001; Mulch et al., 2002; Cosca et al., 2011). Ruffet et al. (1997) noted that  
648 closure of phengites to Ar loss in the EMS is  $\leq 69.4 \pm 0.7$  Ma, which fits well with an Ar loss  
649 event due to fluid flow and deformation in the TSZ at  $\sim 65$  Ma, as determined in this study.

650 Six analyses with a range of apparent  $^{40}\text{Ar}/^{39}\text{Ar}$  ages from 133 to 79 Ma and  
651 inconsistent inverse isochron ages in the felsic mylonite can also be explained by variable  
652 amounts of excess  $^{40}\text{Ar}$ , either derived from relict phengite flakes or from a mixture of  
653 mylonitic and relict phengite (Fig. 5). These age variations of individual grains from a single  
654 hand specimen point to variations in the local Ar pressure and in the network of localized  
655 fluid (Hyodo and York, 1993).

656 Apparent  $^{40}\text{Ar}/^{39}\text{Ar}$  ages in the mafic mylonite (sample MK-99) span a range of  
657 about 30 Ma, and the older dates of  $\sim 99$  Ma and  $\sim 111$  Ma clearly have experienced addition  
658 of excess  $^{40}\text{Ar}$ , as is evident from displacement to lower  $^{36}\text{Ar}/^{40}\text{Ar}$  ratios (Fig. 5). The  
659  $^{40}\text{Ar}/^{36}\text{Ar}$  ratio of the trapped Ar component, i.e. of the mixture of trapped atmospheric and  
660 excess Ar, is  $\sim 417$  for disc MK-99-f. The obtained age of  $81.6 \pm 1.6$  Ma is not very well  
661 defined, but overlaps with phengite core crystallization ages in the EMS and hence suggests  
662 that most of the trapped excess  $^{40}\text{Ar}$  is derived from the HP crystallization period. Although  
663 disc MK-99-DS yields an inverse isochron age ( $62.3 \pm 2.6$  Ma) consistent with mylonitic  
664 phengite from the felsic mylonite, the lack of overlap between apparent  $^{40}\text{Ar}/^{39}\text{Ar}$  spot ages  
665 and inverse isochron age combined with the poor statistical reliability of the inverse isochron  
666 (Table 2) render its reliability doubtful, and may instead be attributed to heterogeneous  
667 incorporation of excess  $^{40}\text{Ar}$ .

668

669

## 670 **6.2. Linking tracers of fluid flow (B, Li, $\delta^{11}\text{B}$ ) with $^{40}\text{Ar}/^{39}\text{Ar}$ data**

671

672 Baxter et al. (2002) stressed that the diffusivity of Ar through an intergranular  
673 transport medium in different lithologies is the key aspect for the accumulation of excess  
674  $^{40}\text{Ar}$ . They introduced the parameter  $t_T$ , the transmissive timescale, which is the time for  $^{40}\text{Ar}$   
675 to escape through the local intergranular transporting medium to some sink for Ar. The  
676 transmissive timescale must be short relative to the timescale of local  $^{40}\text{Ar}$  production to

677 prevent an accumulation of excess  $^{40}\text{Ar}$ . Only rock units with high Ar transmissivities, i.e.  
678 short transmissive timescales, will yield ages that are not affected by excess  $^{40}\text{Ar}$  (Baxter et  
679 al., 2002). Rock units that are being deformed should, in general, be more amenable to dating  
680 as they provide pathways for fast Ar diffusion, which is increased by the presence of a fluid  
681 phase (Cosca et al., 2011; Kramar et al., 2001). In the Tallorno Shear Zone, deformation was  
682 accompanied by fluid flow (Babist et al., 2006; Konrad-Schmolke et al., 2011b), and hence  
683 other chemical tracers of fluid flow are expected to complement the results from the Ar  
684 isotopic analyses.

685

686

#### 687 6.2.1. Limited fluid flow in the weakly deformed EMS unit

688 The low and highly negative  $\delta^{11}\text{B}$  values of the phengite cores are consistent with  
689 preferential loss of  $^{11}\text{B}$  during prograde dehydration and the resulting isotopically light B  
690 isotope signature in dehydrated rocks (Peacock and Hervig, 1999; Bebout, 1999; Wunder et  
691 al., 2005; Marschall et al., 2007). Although isotopic equilibration among nearby samples is  
692 expected because of fluid release by devolatilization reactions at peak pressures (Konrad-  
693 Schmolke et al., 2011a), the significant difference in  $\delta^{11}\text{B}$  of  $\sim 8\text{‰}$  between the phengite cores  
694 of the four EMS samples points to a lack of B isotopic equilibration on the km scale and  
695 limited pervasive fluid flow during phengite crystallization at HP conditions. This agrees well  
696 with previous observations of limited fluid flow during subduction in the internal parts of the  
697 SLZ (Konrad-Schmolke et al., 2006). The lower B contents in phengite cores of the  
698 micaschist point to equilibration with larger amounts of fluid compared to the gneisses, since  
699 the fluid-mobile B is a sensitive indicator for effects of fluid equilibration in the weakly  
700 deformed EMS samples (Konrad-Schmolke et al., 2011b). However, significant influx of  
701 external, slab-derived fluids, which should result in increasing  $\delta^{11}\text{B}$  values, is excluded for  
702 this first overprinting stage ( $\sim 77\text{--}73\text{ Ma}$ ) because the B isotopic composition of the micaschist  
703 falls into the middle of the range exhibited by the gneisses. Hence, phengite core  
704 crystallization in the micaschist is largely dominated by redistribution of B due to percolation  
705 of internally derived fluids (Fig. 7), suggesting that external fluids associated with  
706 deformation and fluid flow in the TSZ did not play a significant role during this stage.

707 This first fluid-induced overprint ( $\sim 77\text{--}73\text{ Ma}$ ) also led to a partial compositional re-  
708 equilibration and the formation of the metasomatized phengite and amphibole rims in the  
709 EMS gneisses (Fig. 7; Konrad-Schmolke et al., 2011a, b). Thermodynamic modeling shows  
710 that the presence of a fluid is required to produce the observed mineral assemblages and

711 mineral chemical modifications on the retrograde  $P$ - $T$  path. The overlap in  $\delta^{11}\text{B}$  values of  
712 relict cores and overprinted rims is consistent with an internally derived fluid, as already  
713 deduced from the micaschist phengite cores that recrystallized contemporaneously. Internally  
714 derived retrograde fluids in HP metasediments can be liberated by a reduction of modal white  
715 mica (Heinrich, 1982). The release of internally derived fluids is also permitted by  
716 thermodynamic models in those regions where the retrograde  $P$ - $T$  path crosses successively  
717 decreasing isopleths of water content bound in minerals. The observed depletion of B and Li  
718 in the phengite rims (Fig. 3) is consistent with this scenario because both Li and B prefer  
719 paragonite over phengite (Marschall et al., 2006a), so that paragonite growth  
720 contemporaneous with the formation of phengite rims (Fig. 2d) would cause a relative  
721 depletion of Li and B in the phengite rims as compared to the corresponding cores. Paragonite  
722 in our samples contains  $\sim 100$ - $120$   $\mu\text{g/g}$  B, consistent with this interpretation. Lithium  
723 concentrations in paragonite are  $\sim 45$   $\mu\text{g/g}$  Li, broadly similar to phengite, but Li is also  
724 preferentially incorporated into newly formed amphibole rims during the overprint. On the  
725 other hand, the influence of an external fluid is indicated at least for the mafic gneiss that  
726 shows a small B isotopic difference (on average  $\sim 3\%$ ) between phengite cores and rims. This  
727 external fluid influx is consistent with the typical lack of retrograde devolatilization reactions  
728 in mafic eclogites (Heinrich, 1982). Results from thermodynamic modeling point to a larger  
729 amount of water influx into the mafic gneiss as compared to the felsic samples during  
730 retrograde metamorphism (Konrad-Schmolke et al, 2011a).

731         The very low fluid/rock ratios that were calculated for the first metasomatic overprint  
732 in the EMS samples (Konrad-Schmolke et al., 2011b) indicate that very little, if any, fluid left  
733 the rock volume, independent of the exact proportions of internally and externally derived  
734 fluids (Fig. 7). The rocks seem to have acted as a sponge, absorbing any fluid diverted from  
735 the TSZ into the EMS country rocks and mixing it with internally produced dehydration-  
736 derived fluids. The limited alteration of the B isotopic compositions agree well with limited  
737 fluid influx, although some redistribution of B and Li occurred during metasomatic  
738 overprinting. Changes in  $X_{\text{Mg}}$  and Si content of phengite (Fig. 2c, d) are in agreement with  
739 fluid-induced recrystallization as these parameters not only depend on changes in  $P$ - $T$   
740 conditions, but also on fluid availability and the phase assemblage during recrystallization.  
741 Hence, oscillatory major-element zonation in phengite can be explained by changes in fluid  
742 availability and cannot be taken as unequivocal evidence for periodic changes in lithostatic  
743 pressure and “yo-yo tectonics” in the SLZ (Rubatto et al., 2011). Fluid-controlled phengite  
744 recrystallization is supported by the observed incorporation of excess  $^{40}\text{Ar}$  in some of the

745 rims. Ar transmissivity remained low where little or no fluid escaped from the rock, and any  
746 available excess  $^{40}\text{Ar}$  could have been redistributed into the rims.

747

748

#### 749 6.2.2. Extensive fluid flow in the Tallorno Shear Zone

750 The mylonitic samples from the TSZ have the highest  $\delta^{11}\text{B}$  values of all investigated  
751 samples and show no isotopic core-rim zonation. This is consistent with the strong major  
752 element re-equilibration and considerable leaching of B and Li during the mylonitic overprint  
753 and the associated fluid influx (Fig. 7). The estimated  $\delta^{11}\text{B}_{\text{fluid}}$  of  $+7 \pm 4 \text{‰}$  is similar to  
754 estimates of slab-derived fluids that entered exhuming HP rocks based on tourmaline  
755 compositions (Bebout and Nakamura, 2003; Altherr et al., 2004; Marschall and Jiang, 2011).  
756 The high- $\delta^{11}\text{B}$  composition of these fluids either reflects subducting altered oceanic materials  
757 or forms by fluid-rock interaction of slab-derived fluids with material in the exhumation  
758 channel during the retrograde evolution (Marschall et al., 2006b; 2009). The observed high  
759  $\delta^{11}\text{B}$  values, therefore, fit well with the geological setting of SLZ, which was located above  
760 the subducting Piemonte Ocean at that time.

761 The difference in  $\delta^{11}\text{B}$  between EMS phengite rims and TSZ mylonitic phengites can  
762 be explained by a different origin and/or a relatively B-poor nature of the fluid. The different  
763 origin is not in contrast to the similar major elemental composition of EMS phengite rims and  
764 TSZ mylonitic phengite, because the presence of a fluid and the same degree of water-  
765 saturation play the major role in determining the phengite compositions at the same  $P$ - $T$   
766 conditions, independent of the fluid origin. If the shear zone fluid interacted with the phengite  
767 rims, its presumed B-poor nature (25 mg/g; Konrad-Schmolke et al., 2011b) would be in  
768 agreement with most B in the rims being inherited from the phengite cores during the  
769 metasomatic overprint. The combination of distinct  $\delta^{11}\text{B}$  values and different  $^{40}\text{Ar}/^{39}\text{Ar}$  ages  
770 demonstrates that two different stages in the metamorphic-metasomatic evolution of this SLZ  
771 are recorded. The B isotopic composition of the TSZ fluid, during the second metasomatic  
772 overprint, was externally controlled, whereas in the EMS there was only limited fluid flow  
773 during the first metasomatic overprint, and the fluid composition was internally controlled by  
774 the rock composition. Rb-Sr data (Babist et al., 2006) bear evidence that the EMS samples  
775 have at least partly been affected by fluid-rock interaction and elemental exchange during  
776 fluid flow and deformation in the shear zone at  $\sim 65$  Ma. However, this event did not  
777 significantly affect the Ar and B isotope systematics.



778           Although B concentrations and  $\delta^{11}\text{B}$  are similar for the felsic and mafic mylonites, the  
779 mafic mylonite (MK-99) lacks any record of the younger events at  $65.0 \pm 3.0$  Ma observed in  
780 the felsic mylonite. Ages and excess  $^{40}\text{Ar}$  contents are lithologically correlated, as observed in  
781 other studies where different ages in spatially adjacent rocks were observed (Baxter et al.,  
782 2002). The young age in the felsic mylonite indicates short transmissive timescales for Ar.  
783 Any inherited  $^{40}\text{Ar}$  was transported away before the mylonitic phengite was closed to Ar  
784 exchange. Yet, the scattered older apparent  $^{40}\text{Ar}/^{39}\text{Ar}$  ages (133–79 Ma) demonstrate that this  
785 transport was not complete. A total lack of apparent  $^{40}\text{Ar}/^{39}\text{Ar}$  ages around 65 Ma coupled to a  
786 significant build-up of excess  $^{40}\text{Ar}$  is observed in the mafic mylonite. This observation, which  
787 is apparently contradicting the re-equilibrated  $\delta^{11}\text{B}$  values, can be explained by exposure of  
788 the mafic mylonite to a grain boundary fluid with high concentrations of excess  $^{40}\text{Ar}$ , as  
789 indicated by the high  $^{40}\text{Ar}/^{36}\text{Ar}$  ratio of the trapped Ar. Thus, the apparent ages in the mafic  
790 mylonite depend on the concentration of excess  $^{40}\text{Ar}$  and/or the extent to which the  $^{40}\text{Ar}/^{36}\text{Ar}$   
791 ratio is greater than the atmospheric ratio in the fluid in equilibrium with the growing  
792 phengite. A similar mechanism was proposed to explain rim ages that were older than core  
793 ages in zoned minerals (Warren et al., 2011). Here, B and Ar isotopes provide complementary  
794 information.

795

796

797

798

## 7. Conclusions

799

800           Using *in situ* UV laser  $^{40}\text{Ar}/^{39}\text{Ar}$  dating, we identified three distinct age periods from  
801 partially overprinted white mica in eclogitic micaschists and mylonites from the Sesia-Lanzo  
802 Zone, Western Alps. By combining the  $^{40}\text{Ar}/^{39}\text{Ar}$  data with B elemental and isotopic analyses,  
803 we linked the age information to fluid-rock interaction processes. Phengite core crystallization  
804 in gneisses from the EMS unit is constrained to 88–82 Ma, a few million years older than  
805 previous estimates of peak *P-T* conditions based on U-Pb zircon geochronology (Rubatto et  
806 al., 2011), but consistent with Rb-Sr isochron data (Oberhänsli et al., 1985). The variation in  
807  $\delta^{11}\text{B}$  among the phengite cores demonstrates a lack of B isotopic equilibration on the km scale  
808 at peak metamorphic conditions. For the petrographically and chemically distinct phengite  
809 rims, younger crystallization ages of 77–73 Ma were obtained. Although there is evidence for  
810 incorporation of excess  $^{40}\text{Ar}$  and Ar loss in some samples, this age agrees well with  
811 crystallization ages of metamorphic zircon rims and vein zircon (Rubatto et al., 1999; 2011).

812 The lower B contents observed in the rims also occur in phengite cores of a micaschist, and  
813 both yield similar  $^{40}\text{Ar}/^{39}\text{Ar}$  ages. Together, they date a first period of metasomatic overprint  
814 in the EMS. The fluid composition during this overprint was largely internally controlled, as  
815 demonstrated by the B data, and B was redistributed among the recrystallizing minerals.  
816 Crystallization of mylonitic phengite in the Tallorno Shear Zone occurred at  $65.0 \pm 3.0$  Ma. In  
817 agreement with high fluid/rock ratios determined for the TSZ, the B isotopic composition of  
818 the TSZ fluid ( $\delta^{11}\text{B} = +7 \pm 4$  ‰) was externally controlled. In summary, the combined Ar and  
819 B isotopic data are accurate enough to discriminate several tectonometamorphic events. The  
820 distribution of apparent  $^{40}\text{Ar}/^{39}\text{Ar}$  ages suggests episodes of HP crystallization and  
821 metasomatic overprinting, lasting several millions of years, rather than discrete events of less  
822 than one million year duration. Phengite crystallization periods can be related to fluid flow  
823 and deformation along the  $P$ - $T$  path experienced by the SLZ rocks.

824

825

## 826 **Acknowledgments**

827 We thank Christine Fischer for help with sample preparation and Fritz Falkenau and Susanne  
828 Schneider for support during SIMS measurements. We also thank the associate editor for  
829 editorial handling and helpful advice, and three anonymous reviewers for their detailed and  
830 constructive comments, which helped to improve the manuscript. Funding of this work by the  
831 Deutsche Forschungsgemeinschaft (grant KO-3750/2-1) is gratefully acknowledged.

832

832 **References**

- 833 Altherr R., Topuz G., Marschall H., Zack T., Ludwig T. (2004) Evolution of a tourmaline-  
834 bearing lawsonite eclogite from the Elekdağ area (Central Pontides, N Turkey): evidence  
835 for infiltration of slab-derived B-rich fluids during exhumation. *Contrib. Mineral. Petrol.*  
836 **148**, 409-425.
- 837
- 838 Arnaud N.O., Kelley S.P. (1995) Evidence for excess argon during high pressure  
839 metamorphism in the Dora Maira Massif (western Alps, Italy), using an ultra-violet laser  
840 ablation microprobe  $^{40}\text{Ar}$ - $^{39}\text{Ar}$  technique. *Contrib. Mineral. Petrol.* **121**, 1-11.
- 841
- 842 Babist J., Handy M.R., Konrad-Schmolke M., Hammerschmidt K. (2006) Precollisional,  
843 multistage exhumation of subducted continental crust: The Sesia Zone, western Alps.  
844 *Tectonics* **25**, TC6008, doi:10.1029/2005TC001927.
- 845
- 846 Baksi A.K. (1999) Reevaluation of plate motion models based on hotspot tracks in the  
847 Atlantic and Indian Oceans. *J. Geol.* **107**, 13-26.
- 848
- 849 Baksi A.K. (2006) Guidelines for assessing the reliability of  $^{40}\text{Ar}/^{39}\text{Ar}$  plateau ages:  
850 Application to ages relevant to hotspot tracks. <http://www.mantleplumes.org/ArAr.html>.
- 851
- 852 Baxter E.F., DePaolo D.J., Renne P.R. (2002) Spatially correlated anomalous  $^{40}\text{Ar}/^{39}\text{Ar}$  “age”  
853 variations in biotites about a lithologic contact near Simplon Pass, Switzerland: A  
854 mechanistic explanation for excess Ar. *Geochim. Cosmochim. Acta* **66**, 1067-1083.
- 855
- 856 Bebout G.E., Nakamura E. (2003) Record in metamorphic tourmalines of subduction-zone  
857 devolatilization and boron cycling. *Geology* **31**, 407-410.
- 858
- 859 Bebout G.E., Ryan J.G., Leeman W.P., Bebout A.E. (1999) Fractionation of trace elements by  
860 subduction-zone metamorphism – effect of convergent-margin thermal evolution. *Earth*  
861 *Planet. Sci. Lett.* **171**, 63-81.
- 862
- 863 Beltrando M., Compagnoni R., Lombardo B. (2010) (Ultra-) High-pressure metamorphism  
864 and orogenesis: An Alpine perspective. *Gondwana Res.* **18**, 147-166.
- 865
- 866 Beltrando M., Lister G.S., Forster M., Dunlap W.J., Fraser G., Hermann J. (2009) Dating  
867 microstructures by the  $^{40}\text{Ar}/^{39}\text{Ar}$  step-heating technique: Deformation-pressure-  
868 temperature-time history of the Penninic Units of the Western Alps. *Lithos* **113**, 801-819.
- 869
- 870 Boundy T.M., Hall C.M., Li G., Essene E.J., Halliday A.N. (1997) Fine-scale isotopic  
871 heterogeneities and fluids in the deep crust: a  $^{40}\text{Ar}/^{39}\text{Ar}$  laser ablation and TEM study of  
872 muscovites from a granulite-eclogite transition zone. *Earth Planet. Sci. Lett.* **148**, 223-  
873 242.
- 874
- 875 Brenan J.M., Ryerson F.J., Shaw H.F. (1998) The role of aqueous fluids in the slab-to-mantle  
876 transfer of boron, beryllium, and lithium during subduction: experiments and models.  
877 *Geochim. Cosmochim. Acta* **62**, 3337-3347.
- 878
- 879 Bröcker M., Baldwin S., Arkudas R. (2013) The geological significance of  $^{40}\text{Ar}/^{39}\text{Ar}$  and  
880 Rb-Sr white mica ages from Syros and Sifnos, Greece: a record of continuous  
881 (re)crystallization during exhumation? *J. metamorphic Geol.* **31**, 629-646.
- 882

- 883 Carrapa B., Wijbrans J. (2003)  $^{40}\text{Ar}/^{39}\text{Ar}$  detrital mica ages in Tertiary sediments shed a new  
884 light on the Eo-Alpine evolution. *J. Virtual Explor.* **13**, 43-55.  
885
- 886 Catanzaro F.J., Champion C.E., Garner E.L., Marinenko G., Sappenfield K.M., Shields W.R.  
887 (1970) Boric acid: isotopic and assay standard reference materials. *Natl. Bur. Stand.*  
888 *Spec. Publ.* **260**, 1-70.  
889
- 890 Channell J.E.T., Hodell D.A., Singer B.S., Xuan C. (2010) Reconciling astrochronological  
891 and  $^{40}\text{Ar}/^{39}\text{Ar}$  ages for the Matuyama-Brunhes boundary and late Matuyama Chron.  
892 *Geochem. Geophys. Geosyst.* **11**, doi:10.1029/2010GC003203.  
893
- 894 Cortiana G., Dal Piaz G.V., Del Moro A., Hunziker J.C., Martin S. (1998)  $^{40}\text{Ar}$ - $^{39}\text{Ar}$  and Rb-  
895 Sr dating of the Pillonet klippe and Sesia-Lanzo basal slice in the Ayas valley and  
896 evolution of the Austroalpine-Piedmont nappe stack. *Mem. Sci. Geol.* **50**, 177-194.  
897
- 898 Cosca M., Stünitz H., Bourgeix A.-L., Lee J.P. (2011)  $^{40}\text{Ar}^*$  loss in experimentally deformed  
899 muscovite and biotite with implications for  $^{40}\text{Ar}/^{39}\text{Ar}$  geochronology of naturally  
900 deformed rocks. *Geochim. Cosmochim. Acta* **75**, 7759-7778.  
901
- 902 Di Vincenzo G., Palmeri R. (2001) An  $^{40}\text{Ar}$ - $^{39}\text{Ar}$  investigation of high-pressure  
903 metamorphism and the retrogressive history of mafic eclogites from the Lanterman  
904 Range (Antarctica): evidence against a simple temperature control on argon transport in  
905 amphibole. *Contrib. Mineral. Petrol.* **141**, 15-35.  
906
- 907 Di Vincenzo G., Ghiribelli B., Giorgetti G., Palmeri R. (2001) Evidence of a close link  
908 between petrology and isotope records: constraints from SEM, EMP, TEM and in situ  
909  $^{40}\text{Ar}$ - $^{39}\text{Ar}$  laser analyses on multiple generations of white micas (Lanterman Range,  
910 Antarctica). *Earth Planet. Sci. Lett.* **192**, 389-405.  
911
- 912 Di Vincenzo G., Carosi R., Palmeri R. (2004) The relationship between tectono-metamorphic  
913 evolution and argon isotope records in white mica: constraints from *in situ*  $^{40}\text{Ar}$ - $^{39}\text{Ar}$  laser  
914 analysis of the Variscan basement of Sardinia. *J. Petrol.* **45**, 1013-1043.  
915
- 916 Di Vincenzo G., Tonarini S., Lombardo B., Castelli D., Ottolini L. (2006) Comparison of  
917  $^{40}\text{Ar}$ - $^{39}\text{Ar}$  and Rb-Sr data on phengites from the UHP Brossasco-Isasca unit (Dora Maira  
918 Massif, Italy): Implications for dating white mica. *J. Petrol.* **47**, 1439-1465.  
919
- 920 Duchêne S., Blichert-Toft J., Luais B., Télouk P., Lardeaux J.-M., Albarède F. (1997) The  
921 Lu-Hf dating of garnets and the ages of the Alpine high-pressure metamorphism. *Nature*  
922 **387**, 586-589.  
923
- 924 Früh-Green G., Scambelluri M., Vallis F. (2001) O-H isotope ratios of high-pressure  
925 ultramafic rocks: Implications for fluid sources and mobility in the subducted hydrous  
926 mantle. *Contrib. Mineral. Petrol.* **141**, 145-159.  
927
- 928 Gebauer D., Grünenfelder M. (1976) U-Pb zircon and Rb-Sr whole rock dating of low-grade  
929 metasediments – Example: Montagne Noire (southern France). *Contrib. Mineral. Petrol.*  
930 **59**, 13-32.  
931

- 932 Giorgis D., Cosca M., Li S. (2000) Distribution and significance of extraneous argon in UHP  
 933 eclogite (Sulu terrain, China): insight from in situ  $^{40}\text{Ar}/^{39}\text{Ar}$  UV-laser ablation analysis.  
 934 *Earth Planet. Sci. Lett.* **181**, 605-615.  
 935
- 936 Hacker B.R., Wang Q. (1995) Ar/Ar geochronology of ultrahigh-pressure metamorphism in  
 937 central China. *Tectonics* **14**, 994-1006  
 938
- 939 Halama R., John T., Herms P., Hauff F., Schenk V. (2011) A stable (Li, O) and radiogenic  
 940 (Sr, Nd) isotope perspective on metasomatic processes in a subducting slab. *Chem. Geol.*  
 941 **281**, 151-166.  
 942
- 943 Hames W.E., Cheney J.T. (1997) On the loss of  $^{40}\text{Ar}^*$  from muscovite during  
 944 polymetamorphism. *Geochim. Cosmochim. Acta* **61**, 3863-3872.  
 945
- 946 Heinrich C.A. (1982) Kyanite-eclogite to amphibolite facies evolution of hydrous mafic and  
 947 pelitic rocks, Adula Nappe, Central Alps. *Contrib. Mineral. Petrol.* **81**, 30-38.  
 948
- 949 Hess J.C., Lippolt H.J. (1994) Compilation of K-Ar measurements on HD-B1 standard biotite  
 950 – 1994 status report. In *Phanerozoic Time Scale (ed. G.S. Odin)*, *Bull. Liais. Inform.*  
 951 *IUGS Subcomm. Geochronol.* **12**, 19-23.  
 952
- 953 Hyodo H., York D. (1993) The discovery and significance of a fossilized radiogenic argon  
 954 wave (argonami) in the Earth's crust. *Geophys. Res. Lett.* **20**, 61-64.  
 955
- 956 Inger S., Ramsbotham W., Cliff R.A., Rex D.C. (1996) Metamorphic evolution of the Sesia-  
 957 Lanzo Zone, Western Alps: time constraints from multi-system geochronology. *Contrib.*  
 958 *Mineral. Petrol.* **126**, 152-168.  
 959
- 960 Ishikawa T., Nakamura E. (1994) Origin of the slab component in arc lavas from across-arc  
 961 variation of B and Pb isotopes. *Nature* **370**, 205-208.  
 962
- 963 Ishizuka O. (1998) Vertical and horizontal variations of the fast neutron flux in a single  
 964 irradiation capsule and their significance in the laser-heating  $^{40}\text{Ar}/^{39}\text{Ar}$  analysis: Case  
 965 study for the hydraulic rabbit facility of the JMTR reactor, Japan. *Geochem. J.* **32**, 243-  
 966 252,  
 967
- 968 Itaya T., Tsujimori T., Liou J.G. (2011) Evolution of the Sanbagawa and Shimanto high-  
 969 pressure belts in SW Japan: Insights from K-Ar (Ar-Ar) geochronology. *J. Asian Earth*  
 970 *Sci.* **42**, 1075-1090.  
 971
- 972 Kelley S. (2002) Excess argon in K-Ar and Ar-Ar geochronology. *Chem. Geol.* **188**, 1-22.  
 973
- 974 Klemme S., Marschall, H.R., Jacob D.E., Prowatke S., Ludwig T. (2011) Trace-element  
 975 partitioning and boron isotope fractionation between white mica and tourmaline. *Can.*  
 976 *Mineral.* **49**, 165-176.  
 977
- 978 Konrad-Schmolke M., Babist J., Handy M.R., O'Brien P.J. (2006) The physico-chemical  
 979 properties of a subducted slab from garnet zonation patterns (Sesia Zone, Western Alps).  
 980 *J. Petrol.* **47**, 2123-2148.  
 981

- 982 Konrad-Schmolke M., O'Brien P.J., Zack T. (2011a) Fluid migration above a subducted slab  
983 – constraints on amount, pathways and major element mobility from partially overprinted  
984 eclogite-facies rocks (Sesia Zone, Western Alps). *J. Petrol.* **52**, 457-486.  
985
- 986 Konrad-Schmolke M., Zack T., O'Brien P., Barth M. (2011b) Fluid migration above a  
987 subducted slab – thermodynamic and trace element modelling of fluid-rock interaction in  
988 partially overprinted eclogite-facies rocks (Sesia Zone, Western Alps). *Earth Planet. Sci.*  
989 *Lett.* **311**, 287-298.  
990
- 991 Kramar N., Cosca M.A., Hunziker J.C. (2001) Heterogeneous  $^{40}\text{Ar}^*$  distributions in naturally  
992 deformed muscovite: in situ UV-laser ablation evidence for microstructurally controlled  
993 intragrain diffusion. *Earth Planet. Sci. Lett.* **192**, 377-388.  
994
- 995 Kuiper Y.D. (2002) The interpretation of inverse isochron diagrams in  $^{40}\text{Ar}/^{39}\text{Ar}$   
996 geochronology. *Earth Planet. Sci. Lett.* **203**, 499-506.  
997
- 998 Kuiper K.F., Deino A., Hilgen F.J., Krijgsman W., Renne P.R., Wijbrans J.R. (2008)  
999 Synchronizing rock clocks of Earth history. *Science* **320**, 500-504.  
1000
- 1001 Lanphere, M.A. (2004) Reply to comment on “Precise K–Ar,  $^{40}\text{Ar}/^{39}\text{Ar}$ , Rb–Sr and U–Pb  
1002 mineral ages from the 27.5 Ma Fish Canyon Tuff reference standard” by M.A. Lanphere  
1003 and H. Baadsgaard. *Chem. Geol.* **211**, 389–390.  
1004
- 1005 Lanphere M.A., Baadsgaard H. (2001) Precise K–Ar,  $^{40}\text{Ar}/^{39}\text{Ar}$ , Rb–Sr and U/Pb mineral ages  
1006 from the 27.5 Ma Fish Canyon Tuff reference standard. *Chem. Geol.* **175**, 653-671.  
1007
- 1008 Lanphere M. A., Dalrymple G.B. (2000) First-principles calibration of  $^{38}\text{Ar}$  tracers:  
1009 Implications for ages of  $^{40}\text{Ar}/^{39}\text{Ar}$  fluence monitors: *U.S. Geological Survey*  
1010 *Professional Paper* **1621**, 1-10.  
1011
- 1012 Lee J.-Y., Marti K., Severinghaus J.P., Kawamura K., Yoo H.-S., Lee J.B., Kim J.S. (2006) A  
1013 redetermination of the isotopic abundances of atmospheric Ar. *Geochim. Cosmochim.*  
1014 *Acta* **70**, 4507-4512.  
1015
- 1016 Marschall H.R., Altherr R., Ludwig T., Kalt A., Gméling K., Kasztovszky Z. (2006a)  
1017 Partitioning and budget of Li, Be and B in high-pressure metamorphic rocks. *Geochim.*  
1018 *Cosmochim. Acta* **70**, 4750-4769.  
1019
- 1020 Marschall H.R., Ludwig T., Altherr R., Kalt A., Tonarini S. (2006b) Syros metasomatic  
1021 tourmaline: evidence for very high- $\delta^{11}\text{B}$  fluids in subduction zones. *J. Petrol.* **47**, 1915-  
1022 1942.  
1023
- 1024 Marschall H.R., Altherr R., Rüpke L. (2007) Squeezing out the slab – modelling the release of  
1025 Li, Be and B during progressive high-pressure metamorphism. *Chem. Geol.* **239**, 323-  
1026 335.  
1027
- 1028 Marschall H.R., Korsakov A.V., Luvizotto G.L., Nasdala L., Ludwig T. (2009) On the  
1029 occurrence and boron isotopic composition of tourmaline in (ultra)high-pressure  
1030 metamorphic rocks. *J. Geol. Soc., London* **166**, 811-823.  
1031

- 1032 Marschall H.R., Jiang S.Y. (2011) Tourmaline isotopes: no element left behind. *Elements* **7**,  
1033 313-319.
- 1034
- 1035 McDougall I., Harrison T.M (1999) Geochronology and thermochronology by the  $^{40}\text{Ar}/^{39}\text{Ar}$   
1036 method. Oxford University Press, New York.
- 1037
- 1038 Mulch A., Cosca M.A., Handy M.R. (2002) In-situ UV-laser  $^{40}\text{Ar}/^{39}\text{Ar}$  geochronology of a  
1039 micaceous mylonite: an example of defect-enhanced argon loss. *Contrib. Mineral. Petrol.*  
1040 **142**, 738-752.
- 1041
- 1042 Nier A.O. (1950) A redetermination of the relative abundances of the isotopes of carbon,  
1043 nitrogen, oxygen, argon, and potassium. *Phys. Rev.* **77**, 789-793.
- 1044
- 1045 Oberhänsli R., Hunziker J.C., Martinotti G., Stern W.B. (1985) Geochemistry, geochronology  
1046 and petrology of Monte Mucrone: An example of eo-Alpine eclogitization of Permian  
1047 granitoids in the Sesia-Lanzo Zone, Western Alps, Italy. *Chem. Geol. (Isot. Geosci. Sect.)*  
1048 **52**, 165-184.
- 1049
- 1050 Pabst S., Zack T., Savov I.P., Ludwig T., Rost D., Tonarini S., Vicenzi E.P. (2012) The fate  
1051 of subducted oceanic slabs in the shallow mantle: Insights from boron isotopes and light  
1052 element composition of metasomatized blueschists from the Mariana forearc. *Lithos* **132-133**,  
1053 162-179.
- 1054
- 1055 Peacock S.M., Hervig R.L. (1999) Boron isotopic composition of subduction-zone  
1056 metamorphic rocks. *Chem. Geol.* **160**, 281-290.
- 1057
- 1058 Putlitz, B, Matthews A., Valley J.W. (2000) Oxygen and hydrogen isotope study of high-  
1059 pressure metagabbros and metabasalts (Cyclades, Greece): implications for the  
1060 subduction of oceanic crust. *Contrib. Mineral. Petrol.* **138**, 114-126.
- 1061
- 1062 Putlitz B., Cosca M.A., Schumacher J.C. (2005) Prograde mica  $^{40}\text{Ar}/^{39}\text{Ar}$  growth ages  
1063 recorded in high pressure rocks (Syros, Cyclades, Greece). *Chem. Geol.* **214**, 79-98.
- 1064
- 1065 Reddy S.M., Kelley S.P., Wheeler J. (1996) A  $^{40}\text{Ar}/^{39}\text{Ar}$  laser probe study of micas from the  
1066 Sesia Zone, Italian Alps: implications for metamorphic and deformation histories. *J.*  
1067 *metamorphic Geol.* **14**, 493-508.
- 1068
- 1069 Regis D., Rubatto D., Darling J., Cenci-Tok B., Zucali M, Engi M. (2013) Multiple  
1070 metamorphic stages within an eclogite-facies terrane (Sesia Zone, Western Alps) revealed  
1071 by U/Th-Pb petrochronology. *J. Petrol.*, in press.
- 1072
- 1073 Renne P. R., Mundil R., Balco G., Min K., Ludwig K.R. (2010) Joint determination of  $^{40}\text{K}$   
1074 decay constants and  $^{40}\text{Ar}^*/^{40}\text{K}$  for the Fish Canyon sanidine standard, and improved  
1075 accuracy for  $^{40}\text{Ar}/^{39}\text{Ar}$  geochronology. *Geochim. Cosmochim. Acta* **74**, 5349-5367.
- 1076
- 1077 Renne P.R., Swisher C.C., Deino A.L., Karner D.B., Owens T.L., DePaolo D.J. (1998)  
1078 Intercalibration of standards, absolute ages and uncertainties in  $^{40}\text{Ar}/^{39}\text{Ar}$  dating. *Chem.*  
1079 *Geol.* **145**, 117-152.
- 1080
- 1081 Rosner M., Erzinger J., Franz G., Trumbull R.B. (2003) Slab-derived boron isotope signatures  
1082 in arc volcanic rocks from the Central Andes and evidence for boron isotope fractionation

1083 during progressive slab dehydration. *Geochem. Geophys. Geosyst* **4**,  
1084 doi:10.1029/2002GC000438.

1085

1086 Rosner M., Wiedenbeck M., Ludwig T. (2008) Composition-induced variations in SIMS  
1087 instrumental mass fractionation during boron isotope ratio measurements of silicate  
1088 glasses. *Geostand. Geoanal. Res.* **32**, 27-38.

1089

1090 Rubatto D., Gebauer D., Compagnoni R. (1999) Dating of eclogite-facies zircons: the age of  
1091 Alpine metamorphism in the Sesia-Lanzo Zone (Western Alps). *Earth Planet. Sci. Lett.*  
1092 **167**, 141-158.

1093

1094 Rubatto D., Regis D., Hermann J., Boston K., Engi M., Beltrando M., McAlpine S.R.B.  
1095 (2011) Yo-yo subduction recorded by accessory minerals in the Italian Western Alps.  
1096 *Nature Geosci.* **4**, 338-342.

1097

1098 Ruffet G., Féraud G., Ballèvre M., Kiénast J.-R. (1995) Plateau ages and excess argon in  
1099 phengites: an  $^{40}\text{Ar}$ - $^{39}\text{Ar}$  laser probe study of Alpine micas (Sesia Zone, Western Alps,  
1100 northern Italy). *Chem. Geol. (Isot. Geosci. Sect.)* **121**, 327-343.

1101

1102 Ruffet G., Gruau G., Ballèvre M., Féraud G., Philippot P. (1997) Rb-Sr and  $^{40}\text{Ar}$ - $^{39}\text{Ar}$  laser  
1103 probe dating of high-pressure phengites from the Sesia zone (Western Alps):  
1104 underscoring of excess argon and new age constraints on the high-pressure  
1105 metamorphism. *Chem. Geol.* **141**, 1-18.

1106

1107 Scaillet S. (1996) Excess  $^{40}\text{Ar}$  transport scale and mechanism in high-pressure phengites: A  
1108 case study from an eclogitized metabasite of the Dora-Maira nappe, western Alps.  
1109 *Geochim. Cosmochim. Acta* **60**, 1075-1090.

1110

1111 Scaillet S., Féraud G., Lagabrielle Y., Ballèvre M., Ruffet G. (1990)  $^{40}\text{Ar}/^{39}\text{Ar}$  laser-probe  
1112 dating by step heating and spot fusion of phengites from the Dora Maira nappe of the  
1113 western Alps, Italy. *Geology* **18**, 741-744.

1114

1115 Scherer E., Münker C., Mezger K. (2001) Calibration of the lutetium-hafnium clock. *Science*  
1116 **293**, 683-687.

1117

1118 Schwarz W.H., Trieloff M. (2007) Intercalibration of  $^{40}\text{Ar}$ - $^{39}\text{Ar}$  age standards NL-25, HB3gr  
1119 hornblende, GA1550, SB-3, HD-B1 biotite and BMus/2 muscovite. *Chem. Geol.* **242**,  
1120 218-231.

1121

1122 Sherlock S.C., Arnaud N.O. (1999) Flat plateau and impossible isochrons: Apparent  $^{40}\text{Ar}$ - $^{39}\text{Ar}$   
1123 geochronology in a high-pressure terrain. *Geochim. Cosmochim. Acta* **63**, 2835-2838.

1124

1125 Sherlock S., Kelley S. (2002) Excess argon evolution in HP-LT rocks: a UVLAMP study of  
1126 phengite and K-free minerals, NW Turkey. *Chem. Geol.* **182**, 619-636.

1127

1128 Smith P.E., York D., Easton R.M., Özdemir Ö., Layer P.W. (1994) A laser  $^{40}\text{Ar}$ - $^{39}\text{Ar}$  study of  
1129 minerals across the Grenville Front: investigation of reproducible excess Ar patterns.  
1130 *Can. J. Earth Sci.* **31**, 808-817.

1131

1132 Sudo M., Uto K., Anno K., Ishizuka O., Uchiumi S. (1998) SORI93 biotite: A new mineral  
1133 standard for K-Ar dating. *Geochem. J.* **32**, 49-58.



- 1134  
1135 Trumbull R., Krienitz M.-S., Grundmann G., Wiedenbeck M. (2009) Tourmaline  
1136 geochemistry and  $\delta^{11}\text{B}$  variations as a guide to fluid-rock interaction in the Habachtal  
1137 emerald deposit, Tauern Window, Austria. *Contrib. Mineral. Petrol.* **157**, 411-427.  
1138
- 1139 Uto K., Ishizuka O., Matsumoto A., Kamioka H., Togashi S. (1997) Laser-heating  $^{40}\text{Ar}/^{39}\text{Ar}$   
1140 dating system of the Geological Survey of Japan: System outline and preliminary results.  
1141 *Bull. Geol. Surv. Japan* **48**, 23-46.  
1142
- 1143 Venturini G., Martinotti G., Armando G., Barbero M., Hunziker J.C. (1994) The Central Sesia  
1144 Lanzo Zone (Western Italian Alps): new field observations and lithostratigraphic  
1145 subdivisions. *Schweiz. Mineral. Petrograph. Mitt.* **74**, 115-125.  
1146
- 1147 Villa I. (1998) Isotopic closure. *Terra Nova* **10**, 42-47.  
1148
- 1149 Warren C.J., Sherlock S.C., Kelley S.P. (2011) Interpreting high-pressure phengite  $^{40}\text{Ar}/^{39}\text{Ar}$   
1150 laserprobe ages: an example from Saih Hatat, NE Oman. *Contrib. Mineral. Petrol.* **161**,  
1151 991-1009.  
1152
- 1153 Warren C.J., Hanke F., Kelley S.P. (2012a) When can muscovite  $^{40}\text{Ar}/^{39}\text{Ar}$  dating constrain  
1154 the timing of metamorphic exhumation? *Chem. Geol.* **291**, 79-86.  
1155
- 1156 Warren C.J., Kelley, S.P., Sherlock S.C., McDonald C.S. (2012b) Metamorphic rocks seek  
1157 meaningful cooling rate: Interpreting  $^{40}\text{Ar}/^{39}\text{Ar}$  ages in an exhumed ultra-high pressure  
1158 terrane. *Lithos* **155**, 30-48.  
1159
- 1160 Warren C.J., Smye A.J., Kelley S.P., Sherlock S.C. (2012c) Using white mica  $^{40}\text{Ar}/^{39}\text{Ar}$  data  
1161 as a tracer for fluid flow and permeability under high-P conditions: Tauern Window,  
1162 Eastern Alps. *J. metamorphic Geol.* **30**, 63-80.  
1163
- 1164 Wiederkehr M., Sudo M., Bousquet R., Berger A., Schmid S.M. (2009) Alpine orogenic  
1165 evolution from subduction to collisional thermal overprint: The  $^{40}\text{Ar}/^{39}\text{Ar}$  age constraints  
1166 from the Valaisan Ocean, central Alps. *Tectonics* **28**, TC6009,  
1167 doi:10.1029/2009TC002496.  
1168
- 1169 Wilke F. D. H., O'Brien P.J., Gerdes G., Timmerman M.J., Sudo M., Khan M.A. (2010) The  
1170 multistage exhumation history of the Kaghan Valley UHP series, NW Himalaya,  
1171 Pakistan from U-Pb and  $^{40}\text{Ar}/^{39}\text{Ar}$  ages. *Eur. J. Mineral.* **22**, 703-719.  
1172
- 1173 Willner A.P., Sepúlveda F.A., Hervé F., Massonne H.-J., Sudo, M. (2009) Conditions and  
1174 timing of pumpellyite-actinolite facies metamorphism in the early Mesozoic frontal  
1175 accretionary prism of the Madre de Dios Archipelago (latitude 50°20'S; Southern Chile).  
1176 *J. Petrol.* **50**, 2127-2155.  
1177
- 1178 Willner A.P., Massonne H.-J., Ring U., Sudo M., Thomson S.N. (2011) P-T evolution and  
1179 timing of a late Palaeozoic fore-arc system and its heterogeneous Mesozoic overprint in  
1180 north-central Chile (latitudes 31-32°S). *Geol. Mag.* **149**, 177-207.  
1181
- 1182 Wunder B., Meixner A., Romer R.L., Wirth R., Heinrich W. (2005) The geochemical cycle of  
1183 boron: Constraints from boron isotope partitioning experiments between mica and fluid.  
1184 *Lithos* **84**, 206-216.  
1185

1185 **Figure captions:**

1186

1187 Fig. 1: (a) Simplified geological map of the Western Alps with the Sesia-Lanzo Zone  
1188 (modified from Beltrando et al., 2010). DB = Dent Blanche, DM = Dora Maira, GP = Gran  
1189 Paradiso, IZ = Ivrea Zone, MR = Monte Rosa, SCZ = Strona-Ceneri Zone, SLZ = Sesia-  
1190 Lanzo Zone. (b) Schematic sampling profile in the Sesia-Lanzo Zone from the Tallorno Shear  
1191 Zone (TSZ) into the EMS unit along the Chiusella Valley (modified from Konrad-Schmolke  
1192 et al., 2011a, b). Note that sample MK-99 is projected onto the cross-section as it was taken  
1193 about 16 km to the NE of sample TSZR.

1194

1195 Fig. 2: (a) Representative back-scattered electron image and (b) major element chemical  
1196 profile through a partially overprinted phengite. In (a), both phengite and sodic amphibole  
1197 show light, relatively Fe-rich rims. The chemical profile in (b) is modified from Konrad-  
1198 Schmolke et al. (2011a). (c) Si compositional map of phengites. The large grain has a pristine  
1199 core and an overprinted rim of variable thickness. On the left side, overprinting has affected  
1200 whole crystals and is not limited to crystal rims. Note that the increase in Si content in  
1201 phengite can be attributed to fluid-induced overprinting. (d) Simplified P-T path with  $X_{Mg}$  in  
1202 phengite for sample MK-52 from the EMS unit (modified from Konrad-Schmolke et al.  
1203 2011a). Peak metamorphic conditions are defined by the assemblage garnet (grt) +  
1204 glaucophane (gln) + clinopyroxene (cpx) + phengite (phe) + quartz (qtz). On the retrograde  
1205 path, the rock passed through the field in the center of the diagram, where paragonite (pg)  
1206 became stable. Note the modeled increase in  $X_{Mg}$  during blueschist-facies overprint, which is  
1207 consistent with the observed mineral chemical zoning (b).

1208

1209 Fig. 3: Variations of B and Li concentrations,  $\delta^{11}B$  and apparent  $^{40}Ar/^{39}Ar$  ages in relict  
1210 phengite cores (black symbols) and overprinted rims (white symbols) from the Eclogitic  
1211 Micaschists and mylonitic phengite (grey symbols) from the Tallorno Shear Zone. (a)  
1212 Moderate loss of B and Li during partial overprint in phengite rims and leaching of both  
1213 elements during fluid infiltration within the TSZ. Boron concentration data are from Konrad-  
1214 Schmolke et al. (2011b). (b) Inversely correlated increase of  $\delta^{11}B$  with decreasing B  
1215 concentrations due to fluid infiltration.  $\delta^{11}B$  values of cores and rims from the EMS samples  
1216 are indistinguishable, indicating limited fluid influx. (c) and (d) show apparent  $^{40}Ar/^{39}Ar$  ages  
1217 with respect to B concentrations and  $\delta^{11}B$ , respectively. Dashed lines connect cores and

1218 overprinted domains from individual samples. In all diagrams, average values with 1 SD as  
1219 error bars are shown.

1220

1221 Fig. 4: Distribution of apparent  $^{40}\text{Ar}/^{39}\text{Ar}$  ages and inverse isochron diagrams for phengites  
1222 from the Eclogitic Micaschists. Vertical arrows in the inverse isochron diagrams indicate  
1223 incorporation of excess  $^{40}\text{Ar}$ . For reference, inverse isochrons with different ages relevant for  
1224 the evolution of the SLZ (85, 75 and 65 Ma) were drawn, using the atmospheric  $^{36}\text{Ar}/^{40}\text{Ar}$   
1225 ratio as y-axis intercept.

1226

1227 Fig. 5: Distribution of apparent  $^{40}\text{Ar}/^{39}\text{Ar}$  ages and inverse isochron diagrams for phengites  
1228 from two mylonites of the Tallorno Shear Zone. Grey diamonds mark data used in the  
1229 calculations of the inverse isochrons, white diamonds are data excluded from the calculations.

1230

1231 Fig. 6: Overview of geochronological data obtained for the Eclogitic Micaschists. The second,  
1232 blueschist-facies overprint at  $65 \pm 3$  Ma is defined based on the inverse isochron age of  
1233 mylonitic mica from the shear zone. The timing of the two earlier crystallization episodes (HP  
1234 crystallization and first overprint) is constrained by the inverse isochron ages of phengite  
1235 cores and overprinted rims. The Lu-Hf age (Duchêne et al., 1997) was recalculated to  $71.6$   
1236  $\pm 2.7$  Ma using the decay constant  $\lambda = 1.865 \times 10^{-11} \text{ year}^{-1}$  (Scherer et al., 2001). Most of the  
1237 Rb-Sr ages (Babist et al., 2006, Inger et al., 1996, and the  $85 \pm 1$  Ma age of Oberhänsli et al.,  
1238 1985) are based on two- or three-point isochrons including phengite. Error bars of single spot  
1239 analyses from this study are omitted for clarity.

1240

1241 Fig. 7: Sketch summarizing the processes relevant for  $^{40}\text{Ar}/^{39}\text{Ar}$  ages, B and Li  
1242 concentrations, and B isotopic compositions of the overprinted phengite rims and the  
1243 recrystallizing mylonitic phengites during metasomatic overprinting. Ages are derived from  
1244 the most reliable inverse isochrons. Deformation and fluid flow in the TSZ causes resetting of  
1245 Ar isotopes, leaching of B and Li, and equilibration of B isotopes with an external fluid. In the  
1246 EMS, B and Li are redistributed resulting in slightly decreasing rim abundances, and B  
1247 isotopes equilibrate internally.

1248

1249 Table 1: Boron isotope analyses of phengites from the Sesia-Lanzo Zone.

1250 Table 2: Summary of  $^{40}\text{Ar}/^{39}\text{Ar}$  age data of the Sesia-Lanzo Zone samples.

1251 Electronic Annex: Results of Ar isotopic analyses measured by UV laser ablation

Fig. 1

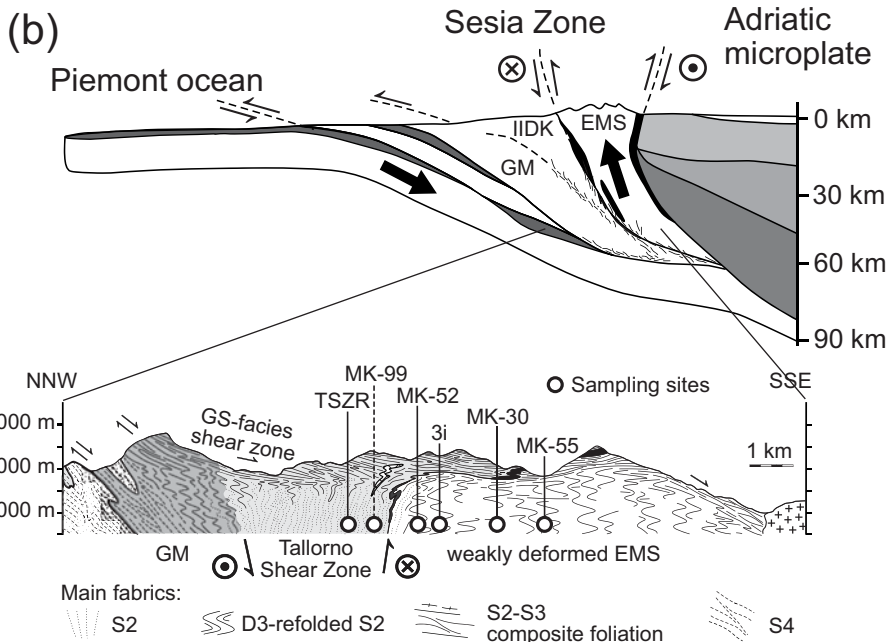
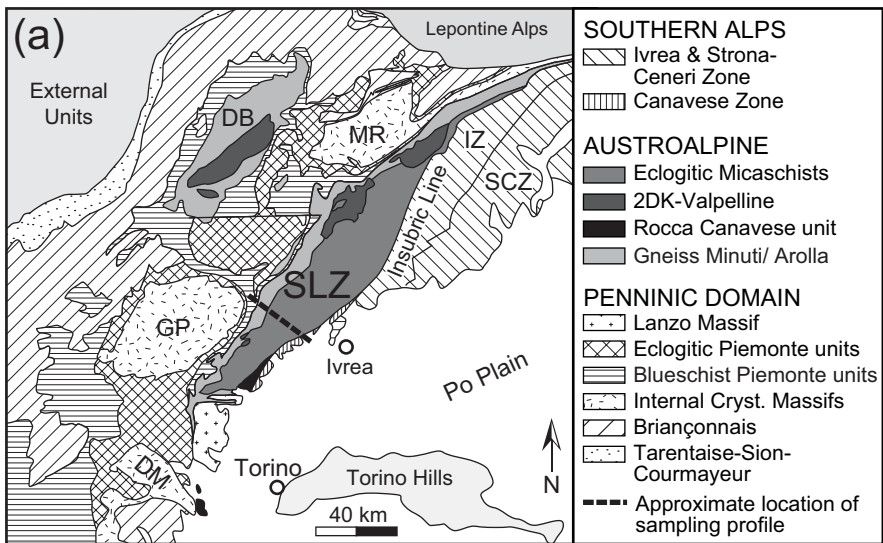


Fig. 2

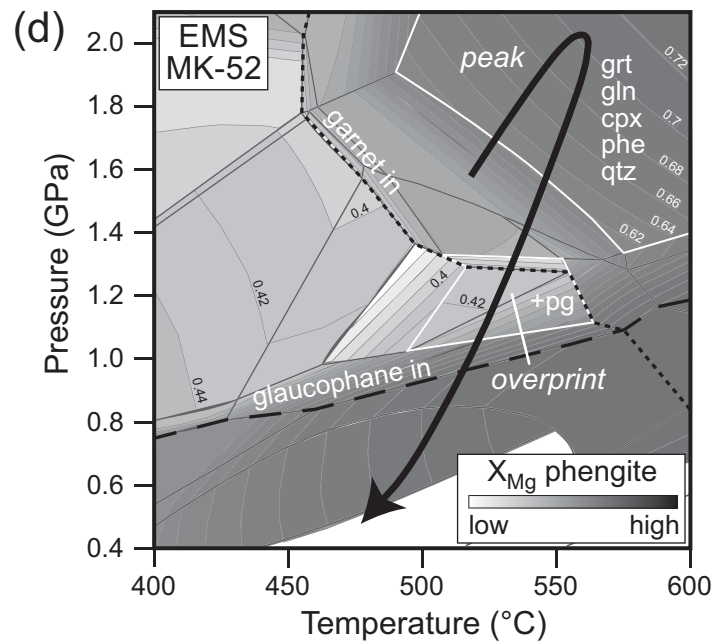
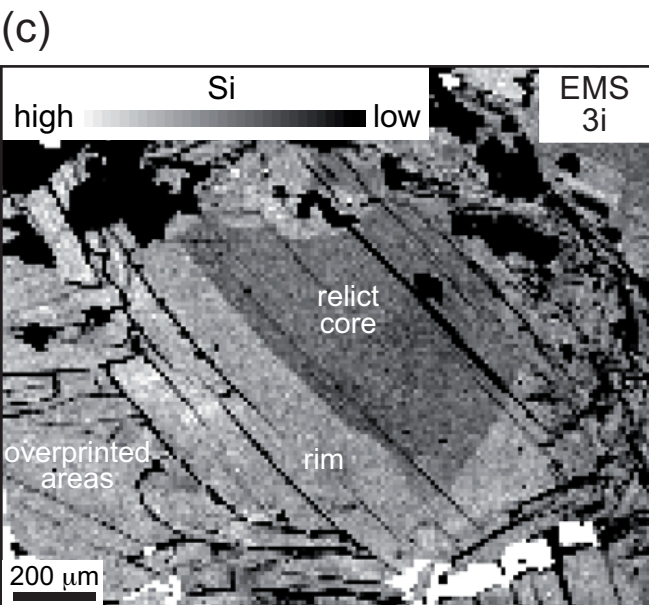
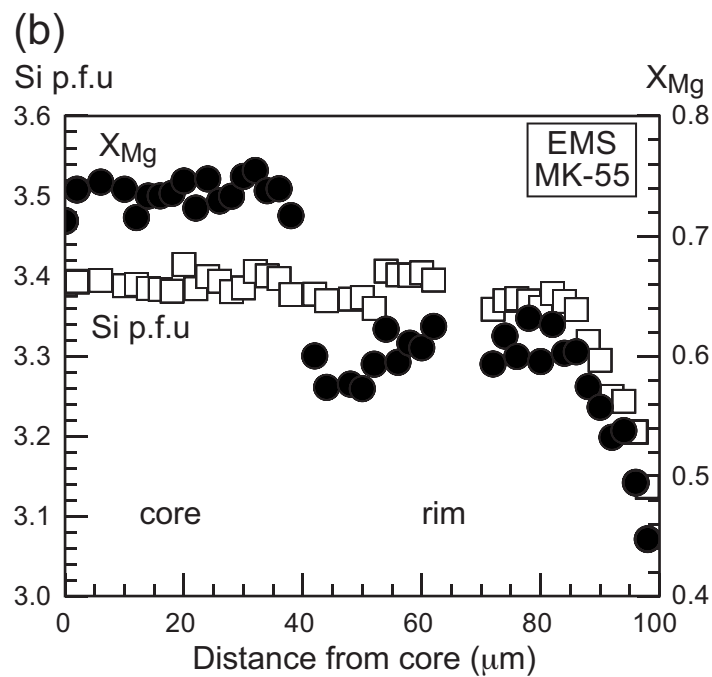
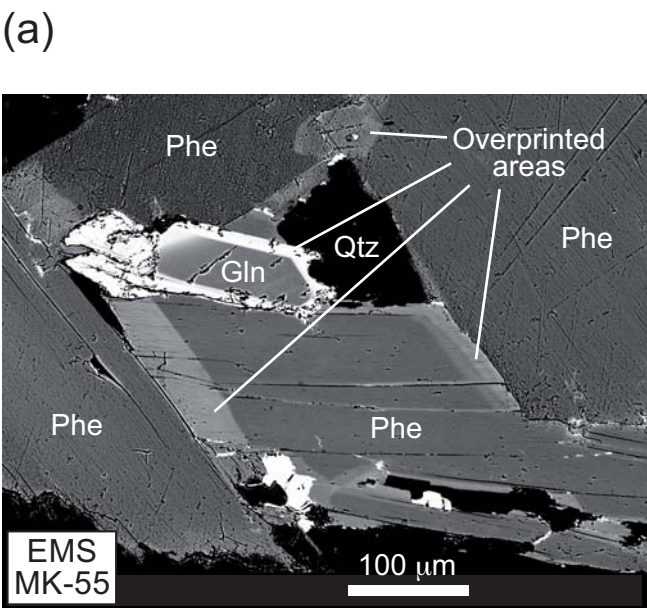


Fig. 3

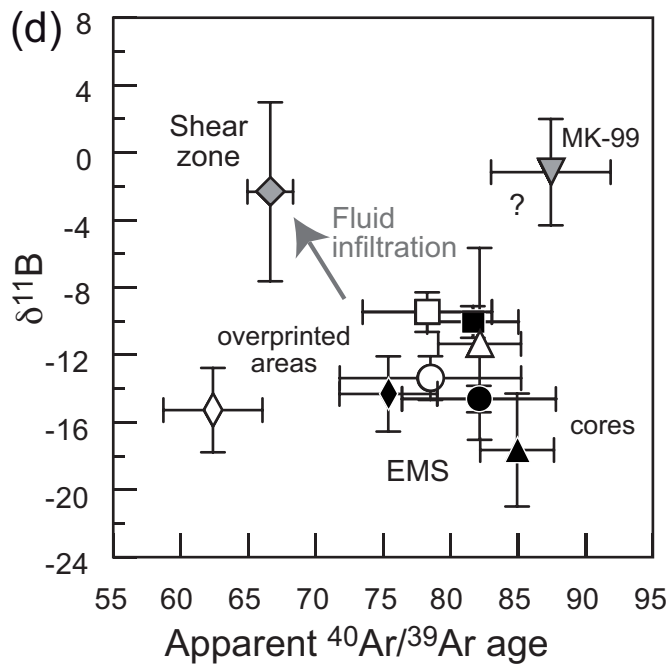
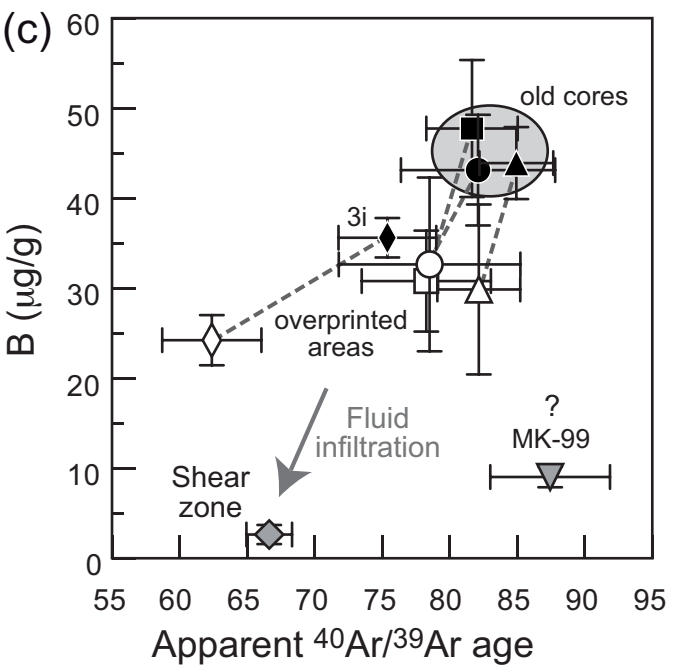
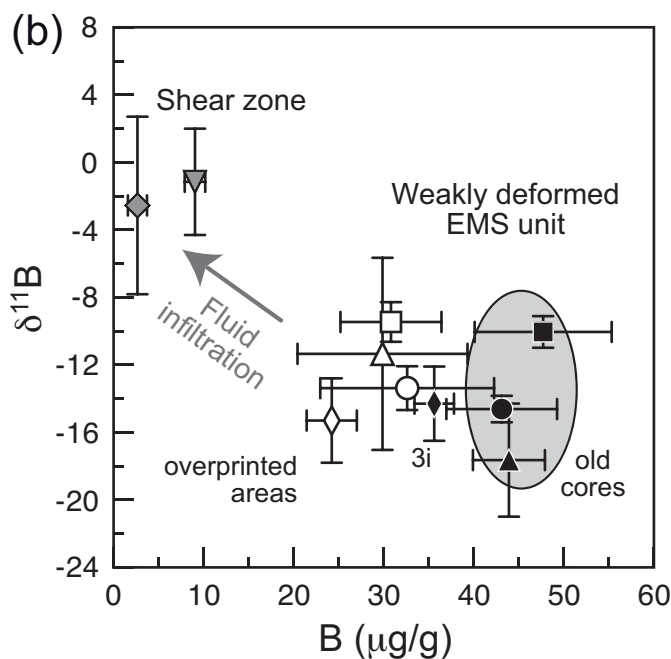
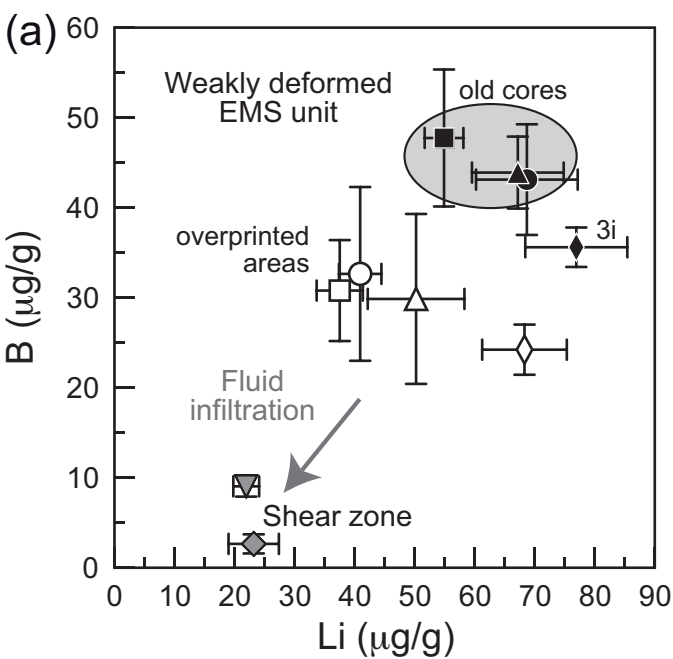


Fig. 4

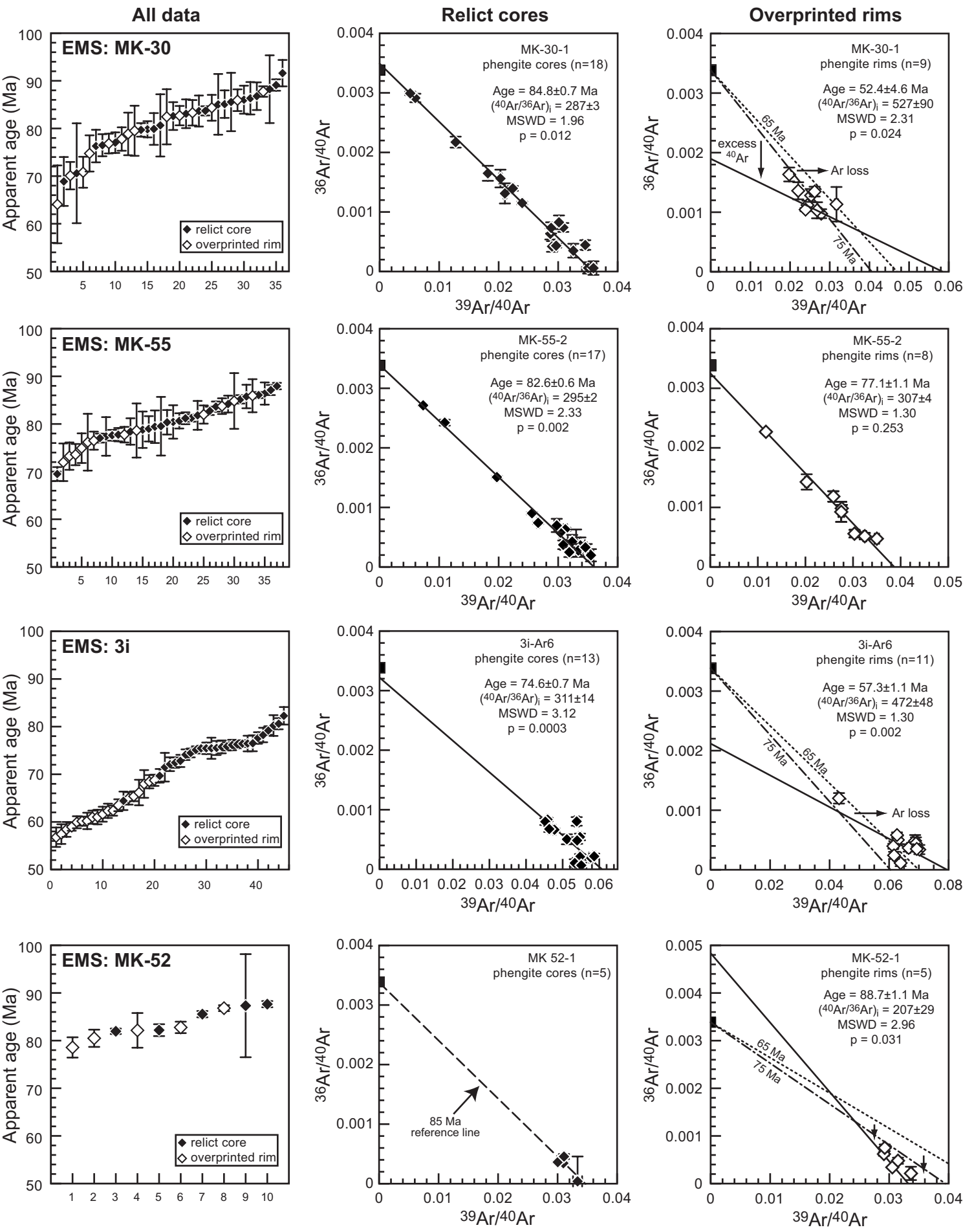


Fig. 5

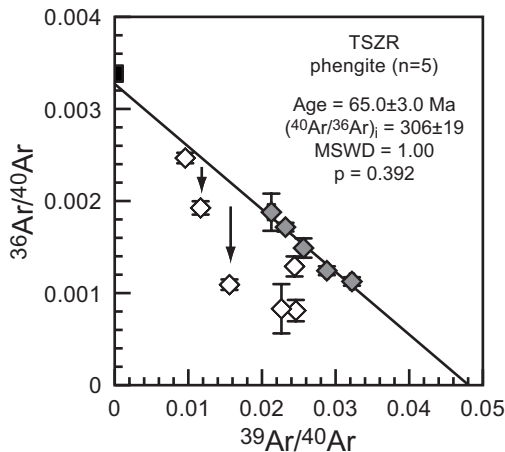
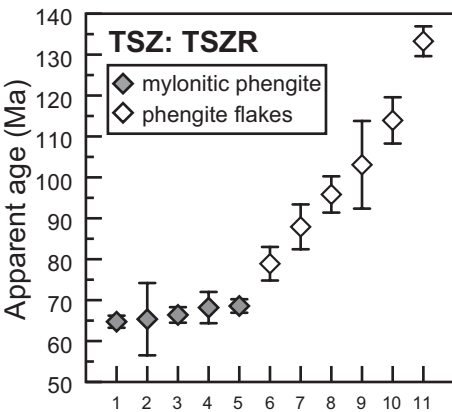
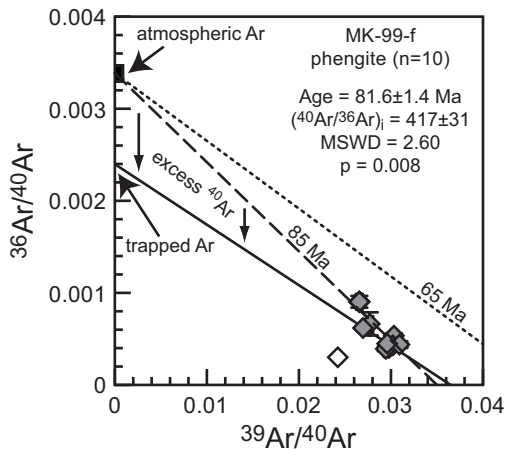
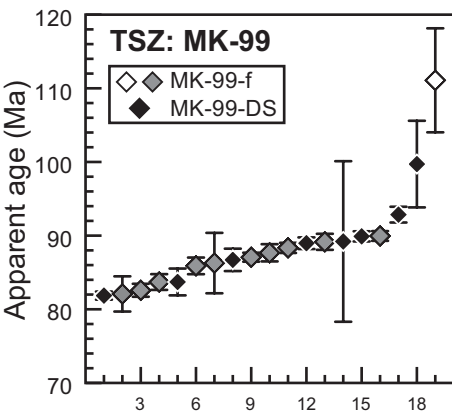




Fig. 6

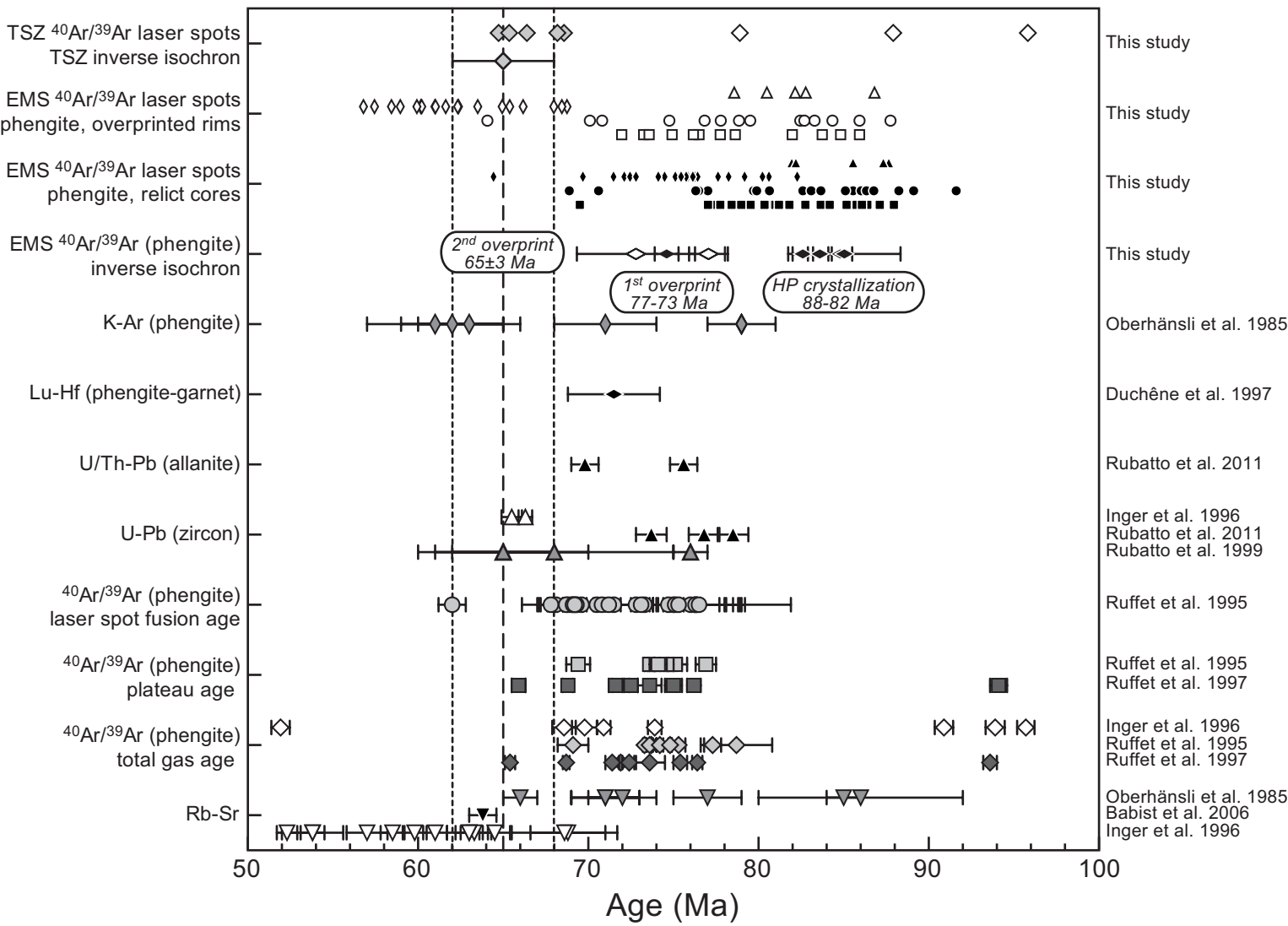


Fig. 7

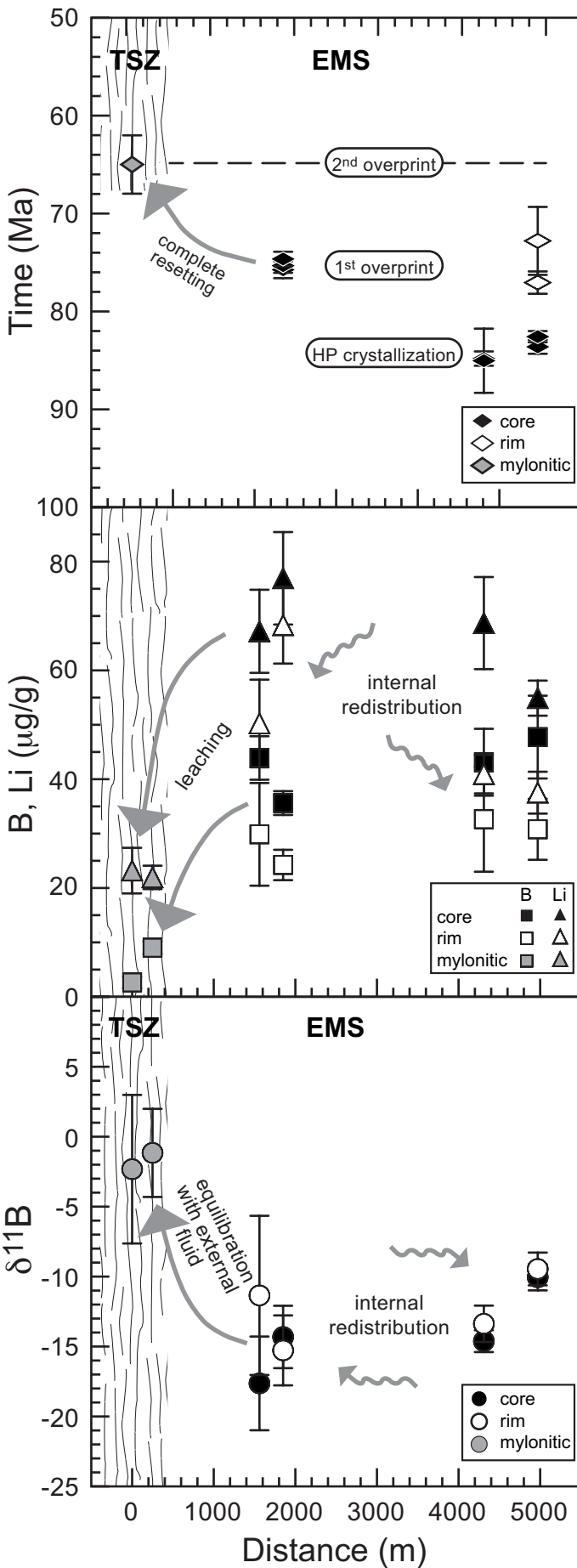


Table 1: Boron isotope analyses of phengites

Analysis #	Position	$\delta^{11}\text{B}$	2s
<b>MK-30, felsic gneiss*</b>			
MK-30-11-2	core	-15.7	1.6
MK-30-11-3	core	-15.0	1.3
MK-30-11-6	core	-14.8	1.6
MK-30-11-8	core	-13.8	1.5
MK-30-11-10	core	-13.6	1.5
MK-30-11-11	core	-14.8	1.8
MK-30-11-1	rim	-13.9	1.5
MK-30-11-4	rim	-12.2	1.8
MK-30-11-5	rim	-11.3	1.8
MK-30-11-7	rim	-14.1	1.9
MK-30-11-9	rim	-13.2	1.8
MK-30-11-12	rim	-13.7	2.1
MK-30-11-13	rim	-15.2	1.8
<b>MK-55, felsic gneiss*</b>			
MK-55-14-1	core	-9.1	1.5
MK-55-14-3	core	-10.0	1.6
MK-55-8-1	core	-11.0	1.6
MK-55-14-2	rim	-8.3	1.8
MK-55-14-4	rim	-9.4	2.4
MK-55-8-2	rim	-10.7	1.8
<b>MK-52, mafic gneiss*</b>			
MK-52-1-1	core	-13.1	1.6
MK-52-1-2	core	-12.7	2.1
MK-52-4-1	core	-18.0	1.6
MK-52-4-2	core	-19.9	1.6
MK-52-6-1	core	-20.3	1.6
MK-52-6-2	core	-20.4	1.6
MK-52-6-5	core	-19.2	1.6
MK-52-1-3	rim	-9.1	2.0
MK-52-1-4	rim	-5.5	2.0
MK-52-1-5	rim	-5.5	2.1
MK-52-4-3	rim	-15.3	1.4
MK-52-6-3	rim	-19.7	1.6
MK-52-6-4	rim	-12.9	1.8
<b>3i, micaschist‡</b>			
30	core	-15.8	1.9
35	core	-13.5	1.1
44	core	-15.8	1.2
36	core	-15.3	1.2
39	core	-15.3	1.1
41	core	-10.1	1.5
31	rim	-14.3	1.4
37	rim	-15.6	1.2
40	rim	-11.2	1.4
32	rim	-19.0	1.0
33	rim	-13.8	1.0
34	rim	-16.9	0.9
38	rim	-16.4	1.7
<b>MK-99, mafic mylonite*</b>			
MK-99-1-1	core	-0.4	3.7
MK-99-1-2	core	-2.0	3.8
MK-99-1-3	core	3.6	3.8
MK-99-1-5	core	-3.1	3.6
MK-99-1-6	core	-2.8	3.6
MK-99-3-2	core	2.0	3.6
MK-99-3-4	core	-1.5	3.5
MK-99-3-5	core	-0.2	3.2
MK-99-1-4	rim	-7.1	3.4
MK-99-3-1	rim	-3.0	3.1
MK-99-3-3	rim	-3.2	3.6
MK-99-3-6	rim	3.8	3.0
<b>TSZR, felsic mylonite‡</b>			
18	core	-10.9	2.8
20	core	-1.0	5.5
24	core	-2.1	5.7
26	core	-7.3	3.7
19	rim	-2.6	4.0
21	rim	2.1	3.9
25	rim	6.2	5.9
27	rim	1.3	4.3
28	rim	-6.7	3.3
22	paragonite	-8.6	3.1
23	paragonite	1.3	3.1

\* analyzed in Heidelberg

‡ analyzed in Potsdam

Table 2: Summary of  $^{40}\text{Ar}/^{39}\text{Ar}$  age data of the Sesia-Lanzo Zone samples

Location	# of spots	Comment	Apparent spot ages		Apparent spot ages		Inverse isochron age	$(^{40}\text{Ar}/^{36}\text{Ar})_i$	MSWD	$\chi^2$	p
			AVG	STDEV	Wt. AVG	Error					
<b>EMS, MK-30, felsic gneiss</b>											
MK-30-1 cores	18	all	81.9 ± 6.1		83.6 ± 0.5		84.8 ± 0.7	287 ± 3	1.96	31.36	0.012
MK-30-2 cores	4	all	83.2 ± 3.9		81.6 ± 1.1		85.0 ± 3.3	243 ± 57	1.86	3.72	0.156
MK-30-1 rims	9	all	77.6 ± 7.2		83.3 ± 0.8		52.4 ± 4.6	527 ± 90	2.31	16.17	0.024
MK-30-2 rims	5	all	80.1 ± 6.2		80.9 ± 1.1		80.2 ± 2.2	308 ± 43	2.64	7.92	0.048
<b>EMS, MK-55, felsic gneiss</b>											
MK-55-1 cores	7	all	82.8 ± 3.7		84.0 ± 0.4		83.6 ± 0.7	314 ± 13	4.70	23.50	0.000
MK-55-2 cores	17	1 excluded	81.2 ± 3.3		82.3 ± 0.4		82.6 ± 0.6	295 ± 2	2.33	35.02	0.002
MK-55-1 rims	4	all	76.9 ± 6.3		76.2 ± 1.6		72.8 ± 3.5	388 ± 118	2.22	4.44	0.109
MK-55-2 rims	8	all	79.0 ± 4.2		79.3 ± 0.8		77.1 ± 1.1	307 ± 4	1.30	7.80	0.253
<b>EMS, MK-52, mafic gneiss</b>											
cores	5	all	84.9 ± 2.7		84.6 ± 0.3		— —	— —	—	—	—
rims	5	all	82.2 ± 3.1		85.0 ± 0.5		88.7 ± 1.1	207 ± 29	2.96	8.88	0.031
<b>EMS, 3i, micaschist</b>											
3i-Ar-4-05 cores	5	all	76.0 ± 3.1		75.9 ± 0.5		75.8 ± 0.9	299 ± 15	1.60	4.80	0.187
3i-Ar-4-10 cores	8	all	75.7 ± 1.7		75.9 ± 0.4		75.3 ± 0.7	412 ± 85	1.81	10.88	0.092
3i-Ar-6-06 cores	13	all	74.9 ± 4.7		75.2 ± 0.4		74.6 ± 0.7	311 ± 14	3.12	34.31	0.000
3i-Ar-4-10 rims	8	all	62.6 ± 2.2		62.4 ± 0.5		60.2 ± 1.4	442 ± 102	1.23	7.41	0.285
3i-Ar-6-06 rims	11	all	61.7 ± 4.4		62.0 ± 0.4		57.3 ± 1.1	472 ± 48	2.95	26.59	0.002
<b>TSZ, MK-99, mafic mylonite</b>											
MK-99-f mylonitic	10	1 excluded	86.3 ± 2.7		87.2 ± 0.3		81.6 ± 1.4	417 ± 31	2.60	20.80	0.008
MK-99-DS mylonitic	8	all	89.1 ± 5.5		86.6 ± 0.3		62.3 ± 2.6	954 ± 114	2.80	16.80	0.010
<b>TSZ, TSZR, felsic mylonite</b>											
mylonitic phengite	5	selection 1	66.6 ± 1.7		66.5 ± 0.9		65.0 ± 3.0	306 ± 19	1.00	3.00	0.392
phengite flakes	6	selection 2	102.2 ± 19.5		104.3 ± 2.0		100.2 ± 3.0	315 ± 10	5.44	21.76	0.000